The Journal of
Undergraduate Research
in Physics

CONTENTS

Volume 18, Number 1
Winter, 1999

Produced by the Physics Department of Guilford College
for
The American Institute of Physics and the Society of Physics Students

THE JOURNAL OF UNDERGRADUATE RESEARCH IN PHYSICS

This journal is devoted to research work done by undergraduate students in physics and its related fields. It is a vehicle for the exchange of ideas and information by undergraduate students. Information for students wishing to submit manuscripts for possible inclusion in the Journal follows.

ELIGIBILITY
The author(s) must have performed all work reported in the paper as an undergraduate student(s). The subject matter of the paper is open to any area of pure or applied physics or physics related field.

SPONSORSHIP
Each paper must be sponsored by a full-time faculty member of the department in which the research was done. A letter from the sponsor, certifying that the work was done by the author as an undergraduate and that the sponsor is willing to be acknowledged at the end of the paper, must accompany the manuscript if it is to be considered for publication.

SUBMISSION
Two copies of the manuscript, the letter from the sponsor and a telephone number or E-Mail address where the author can be reached should be sent to:
Dr. Rexford E. Adelberger, Editor
THE JOURNAL OF UNDERGRADUATE RESEARCH IN PHYSICS
Physics Department
Guilford College
Greensboro, NC 27410

FORM
The manuscript should be typed, double spaced, on 8 1/2 x 11 inch sheets. Margins of about 1.5 inches should be left on the top, sides, and bottom of each page. Papers should be limited to fifteen pages of text in addition to an abstract (not to exceed 250 words) and appropriate drawings, pictures, and tables. Manuscripts may be submitted on a disk or as an E-mail attachment that can be read by a MacIntosh™. The files must be compatible with MicroSoft Word™ or PageMaker™.

ILLUSTRATIONS
Line drawings should be made with black ink on plain white paper. The line thickness should be sufficient to be reduced to column format. Each figure or table must be on a separate sheet. Photographs must have a high gloss finish. If the submission is on a disk, the illustrations should be in PICT, TIFF or EPS format.

CAPTIONS
A descriptive caption should be provided for each illustration or table, but it should not be part of the figure. The captions should be listed together at the end of the manuscript

EQUATIONS
Equations should appear on separate lines, and may be written in black ink. All equations should be numbered. We use EXPRESSIONIST™ to format equations in the Journal.

FOOTNOTES
Footnotes should be typed, double spaced and grouped together in sequence at the end of the manuscript.

PREPARING A MANUSCRIPT
A more detailed set of instructions and advice for authors wishing to prepare manuscripts for publication in the Journal of Undergraduate Research in Physics can be found in the back of each issue.

SUBSCRIPTION INFORMATION

The Journal is published twice each academic year, issue # 1 appearing in the fall and issue # 2 in the spring of the next calendar year. There are two issues per volume.

TYPE OF SUBSCRIBER	PRICE PER VOLUME
Individual	$US 5.00
Institution	$US 10.00

Foreign subscribers add $US 2.00 for surface postage, $US 10.00 for air freight.

Back issues may be purchased by sending $US 15.00 per volume to the editorial office.

To receive a subscription, send your name, address, and check made out to **The Journal of Undergraduate Research in Physics (JURP)** to the editorial office:

JURP
Physics Department
Guilford College
Greensboro, NC 27410

The Journal of Undergraduate Research in Physics is sent to each member of the Society of Physics Students as part of their annual dues.

VOLUME 18

ACADEMIC YEAR 1999-2000

The Journal of Undergraduate Research in Physics

Produced by the Physics Department
of Guilford College
for
The American Institute of Physics
and
The Society of Physics Students

ISSN 0731 - 3764

A SELF-CONSISTENT APPROACH TO THE LASER COOLING OF V-TYPE ATOMS

Anthony Williams*
Department of Chemistry and Physics
Rowan University
Glassboro, NJ 08080
received April 30, 1999

ABSTRACT

The equations of motion for three energy level V-type atoms driven by two counter propagating laser fields are derived from Schrödinger's equation. These equations at steady state are reduced to a single integral equation for the ground state momentum distribution. A numerical method, based on a self-consistent approach, is developed to study the laser cooling of V-type atoms. A good agreement is reached between our numerical results and those from existing theory. [1]

[1] Y. Castin, H. Wallis, and J. Dalibard, J. Opt. Am., B 6, (1989), p. 2046.

INTRODUCTION

A single photon has a momentum $\hbar k$ and has an energy $\hbar\omega$, where $\hbar$ is Planck's constant divided by 2π and k is the wave number and ω is the frequency of the electromagnetic field of the photon. Due to momentum conservation, an atom of mass M and momentum p can gain or lose momentum of $\hbar k$ during the absorption or emission of a single photon. Consequently, the kinetic energy of the atom changes by:

$$\frac{(p \pm \hbar k)^2}{2M} - \frac{p^2}{2M} = \frac{\pm \hbar k p}{M} + E_r , \qquad (1)$$

where kp/M is the Doppler frequency shift and E_r is the atomic recoil energy:

$$E_r = \frac{(\hbar k)^2}{2M} = \hbar\omega_r , \qquad (2)$$

were ω_r is called the recoil frequency shift. These ideas form the basis for the laser cooling of atoms. [1]

Temperature is a measure of the average kinetic energy of the atoms in a system. The average kinetic energy is determined by the atomic momentum (or velocity) distribution. Atoms in thermal equilibrium follow the Maxwell-Boltzmann distribution; the broader the distribution the higher the temperature. The essential task of laser cooling is to narrow the momentum distribution profile by an exchange of momentum between atoms and photons. The simplest laser cooling scheme is when atoms of two energy levels are driven by two opposing laser fields of the same frequency. The Doppler effect causes the atoms to see the laser beam traveling in the direction opposite to their motion to have a higher frequency than that along their direction of motion. If the laser frequency is less than the atomic transition frequency and the motion of the atoms are slow enough, the frequency shift due to the Doppler effect will always bring the energy of the counter propagating laser closer to energy of the atomic transition than the copropagating one. As a result, the radiation force

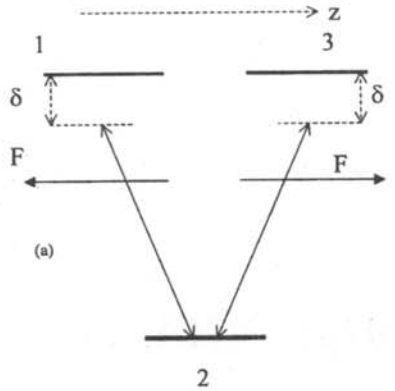

Figure 1
A schematic diagram of three-level 'V' type atoms driven by two counter propagating laser fields of amplitude F, and frequency detuning δ. The system is oriented along the z axis.

The author graduated from Rowan University in May with a B.Sc. in mathematics and physics. He accepted an offer to attend physics graduate school at the University of Notre Dame. The work was presented at the 1999 National Conference of Undergraduate Research. His outside interests include paintball, flag football and helping his father with his race car.

given to the atom by counter propagating laser is always larger than that given by the copropagating laser. This effect gives rise to a net force opposing the motion of the atoms, and results in the narrowing of the momentum distribution of the atoms and the reduction of the atomic temperature.

A V-type atom, the kind that is discussed in this paper, is a three energy level atom whose levels are arranged in a 'V' as shown in Figure 1. The transitions between the quantum states 1 -> 2 and 3 -> 2 are driven independently by two counter propagating laser fields of the same amplitude F, frequency ω and wave number k. We are interested in momentum distribution of the 'cooled' atoms, both in the broad distribution ($\Delta p >> \hbar k$) and narrow distribution ($\Delta p \approx \hbar k$), where Δp is the width of the atomic momentum distribution. In the case of the narrow momentum distribution, the deBroglie wavelength of the atom, $\lambda_D = h/p \approx h/\hbar k = 2\pi/k = \lambda$ is on the order of the wavelength of the laser field. In this case, the atoms can no longer be viewed as localized particles moving classically under the electromagnetic fields of the lasers.

A more accurate theoretical description requires the simultaneous quantization of both the internal and external (center-of-mass) degrees of freedom. In a theory developed for the 'V' system, the steady-state momentum distribution is obtained either by integrating the generalized Optical Bloch (GOB) equation over a long period of time or solving directly the steady-state coupled GOB equations. [2] The former is very time consuming, while the latter involves matrices of large dimension. In this work, we approach this problem in a self-consistent manner. In a self-consistent approach, we start from a guessed function and use the equation of interest to arrive at an improved solution in an iterative manner until the solution does not appear to change with further iteration. This method is easy to implement and quite efficient for atoms with narrow atomic lines.

EQUATIONS OF MOTION

The time dependent Schrödinger equation for this system is:

$$i\hbar\frac{\partial}{\partial t}|\psi> = \left(\hat{H}_A + \frac{1}{2}\frac{\hat{p}^2}{M} + \hat{H}_{AL}\right)|\psi>, \qquad (3)$$

where $\hat{H}_A$ represents the interaction among the particles inside the atom, $\frac{1}{2}\frac{\hat{p}^2}{M}$ is the kinetic energy of the center-of-mass and $\hat{H}_{AL}$ is the dipole interaction between the atom and the laser fields. The interaction of the atoms with the vacuum is not included in Equation 3 but will be introduced later phenomenologically. We choose to work in a space spanned by $|i,p>$, defined as:

$$\hat{H}_A\,|i,p> = \hbar\,\Omega_{i2}\,|i,p>$$
$$\hat{p}\,|i,p> = p\,|i,p> \quad , \qquad (4)$$

where $\hbar\,\Omega_{i2}$ is the energy of the i^{th} level relative to the ground state energy and p is the eigenvalue of the momentum operator. The system is closed in the sense that:

$$\int_{-\infty}^{+\infty}\sum_{n=1}^{3}|i,p><i.p|\,dp = 1\,. \qquad (5)$$

The dipole interaction is given by:

$$\hat{H}_{AL} = -\hat{\mu}\cdot\hat{F}\,, \qquad (6)$$

where the electric dipole momentum operator is:

$$\hat{\mu} = e\,\hat{r}_e\,, \qquad (7)$$

where e is the charge of the electron and $\hat{r}_e$ is the position operator for the electron, and the total field operator is given by

$$\hat{F}(\hat{z},t) = \frac{1}{2}\left(\vec{e}_{32}F\,e^{-i\omega t+ik\hat{z}} + \vec{e}_{12}F\,e^{-i\omega t-ik\hat{z}}\right) + \frac{1}{2}\left(\vec{e}_{32}F^{*}\,e^{i\omega t-ik\hat{z}} + \vec{e}_{12}F^{*}\,e^{i\omega t+ik\hat{z}}\right), \qquad (8)$$

where $\vec{e}_{32}$ and $\vec{e}_{12}$ are the polarizations of the forward and backward laser fields. The dipole moment operator only affects the internal quantum numbers of the atom. In our system, the two laser fields are polarized in such a way that:

$$<3|\hat{\mu}\cdot\vec{e}_{32}|2> = <1|\hat{\mu}\cdot\vec{e}_{12}|2> \equiv \mu \qquad (9)$$

are the only nonzero matrix elements.

To find the matrix expansion of the dipole interaction, we make use of the identity:

$$e^{+ik\hat{z}}|i,p> = |i,p+\hbar k>\,. \qquad (10)$$

Equation 10 can be proved using the transformation between position and momentum space which can be found in many quantum mechanic textbooks: [3]

$$|i,p> = \frac{1}{\sqrt{2\pi\hbar}}\int_{-\infty}^{+\infty}e^{i\frac{pz}{\hbar}}|i,z>\,dz\,, \qquad (11)$$

Operating on both sides of Equation 11 with $e^{+ik\hat{z}}$ yields:

$$e^{+ik\hat{z}}|i,p> = \frac{1}{\sqrt{2\pi\hbar}}\int_{-\infty}^{+\infty}e^{i\frac{(p+\hbar kz)}{\hbar}}|i,z>\,dz = |i,p+\hbar k>, \qquad (12)$$

Using the identity of Equation 10 and substituting Equation 8 into Equations 6 gives the matrix elements of the dipole interaction as:

$$\begin{aligned}
\hat{H}_{AL}|1,p> &= -\hbar E e^{-i\omega t}|2,p-\hbar k> - \hbar E^{*}e^{i\omega t}\,|2,p+\hbar k>\\
\hat{H}_{AL}|2,p> &= -\hbar E e^{-i\omega t}|3,p+\hbar k> - \hbar E^{*}e^{i\omega t}\,|3,p-\hbar k>\\
&\quad -\hbar E e^{-i\omega t}|1,p-\hbar k> - \hbar E^{*}e^{-i\omega t}\,|1,p+\hbar k> \qquad (13)\\
\hat{H}_{AL}|3,p> &= -\hbar E e^{-i\omega t}|2,p+\hbar k> - \hbar E^{*}e^{-i\omega t}\,|2,p-\hbar k>\,,
\end{aligned}$$

where $E=\mu F/2\hbar$ is called the Rabi frequency of the laser field. [5]

Expanding the wave function in terms of the slowly varying dynamical variable $c_i(p,t)$ gives:

$$|\psi> = \int \left[\begin{array}{c} c_1(p,t)e^{-i\omega t}|1,p> + c_2(p,t)|2,p> \\ + c_3(p,t)e^{-i\omega t}|3,p> \end{array} \right] dp \qquad (14)$$

The second term does not have a time dependence since it represents the ground state of the 'V' atom. Inserting Equation 14 into Equation 3 and ignoring terms proportional to $e^{\pm i2\omega t}$ (the so-called rotational wave approximation [5]) we find a closed set of equations:

$$\begin{aligned} \frac{d}{dt}c_2(p,t) &= -i\frac{p^2}{2M\hbar}c_2(p,t) - iE^* c_1(p-\hbar k,t) \\ &\quad - iE^* c_3(p+\hbar k,t) \\ \frac{d}{dt}c_1(p-\hbar k,t) &= +i\left[\delta - \frac{(p-\hbar k)^2}{2M\hbar}\right] c_1(p-\hbar k,t) \\ &\quad + iEc_2(p,t) \\ \frac{d}{dt}c_3(p+\hbar k,t) &= +i\left[\delta - \frac{(p+\hbar k)^2}{2M\hbar}\right] c_3(p+\hbar k,t) \\ &\quad + iEc_2(p,t)\,, \end{aligned} \qquad (15)$$

where:

$$\delta = \omega - \Omega_{32} - \omega_r = \omega - \Omega_{12} - \omega_r$$

is the laser detuning with respect to the recoil frequency shift.

The momentum distribution of the atoms is associated with $c_2(p,t)c_2^*(p,t)$. To form a closed set of equations such as Equations 15 involving the atomic momentum distribution, we introduce the density matrix elements:

$$\begin{aligned} \rho_{11}(p,t) &= c_1(p-\hbar k,t)c_1^*(p-\hbar k,t) \\ \rho_{22}(p,t) &= c_2(p,t)c_2^*(p,t) \\ \rho_{33}(p,t) &= c_3(p+\hbar k,t)c_3^*(p+\hbar k,t) \\ \rho_{21}(p,t) &= c_2(p,t)c_1^*(p-\hbar k,t) \\ \rho_{32}(p,t) &= c_3(p+\hbar k,t)c_2^*(p,t) \\ \rho_{13}(p,t) &= c_1(p-\hbar k,t)c_3^*(p+\hbar k,t) \\ \rho_{ij}(p,t) &= \rho_{ji}^*(p,t) \quad i \neq j \end{aligned} \qquad (16)$$

If we take spontaneous emission into consideration, we find that the equations of motion for the density matrix elements are governed by Equations 17, known for historical reasons as the GOB: [2,5]

$$\begin{aligned} \frac{d}{dt}\rho_{11}(p,t) &= -\Gamma\rho_{11}(p,t) + i\left[E\rho_{21}(p,t) - E^*\rho_{12}(p,t)\right] \\ \frac{d}{dt}\rho_{33}(p,t) &= -\Gamma\rho_{33}(p,t) + i\left[E\rho_{23}(p,t) - E^*\rho_{32}(p,t)\right] \\ \frac{d}{dt}\rho_{12}(p,t) &= -\left[0.5\Gamma - i\delta'_{12}(p)\right]\rho_{12}(p,t) + \\ &\quad iE\left[\rho_{22}(p,t) - \rho_{11}(p,t)\right] - iE\rho_{13}(p,t) \\ \frac{d}{dt}\rho_{32}(p,t) &= -\left[0.5\Gamma - i\delta'_{32}(p)\right]\rho_{32}(p,t) + \\ &\quad iE\left[\rho_{22}(p,t) - \rho_{33}(p,t)\right] - iE\rho_{31}(p,t) \\ \frac{d}{dt}\rho_{31}(p,t) &= -\left[\Gamma - i\delta'_{31}(p)\right]\rho_{31}(p,t) + \\ &\quad i\left[E\rho_{21}(p,t) - E^*\rho_{32}(p,t)\right] \\ \frac{d}{dt}\rho_{22}(p,t) &= \Gamma\int_{-\hbar k}^{+\hbar k} dq\, N(q)\,\rho_{11}(p+\hbar k+q,t) + \\ &\quad \Gamma\int_{-\hbar k}^{+\hbar k} dq\, N(q)\,\rho_{33}(p-\hbar k+q,t) - \\ &\quad i\left[E\rho_{21}(p,t) - E^*\rho_{12}(p,t)\right] - i\left[E\rho_{23}(p,t) - E^*\rho_{32}(p,t)\right], \\ \frac{d}{dt}\rho_{21}(p,t) &= \frac{d}{dt}\rho_{12}^*(p,t) \\ \frac{d}{dt}\rho_{23}(p,t) &= \frac{d}{dt}\rho_{32}^*(p,t) \\ \frac{d}{dt}\rho_{13}(p,t) &= \frac{d}{dt}\rho_{31}^*(p,t) \end{aligned} \qquad (17)$$

where Γ is the decay rate of the excited state, $N(q)$ is the probability of an excited atom of momentum $p+q$, where $|q| \leq \hbar k$, becoming a ground state atom with momentum p and:

$$\begin{aligned} \delta'_{12}(p) &= \delta + \frac{k}{M}p = \delta + 2\,\omega_r\frac{p}{\hbar k} \\ \delta'_{32}(p) &= \delta - \frac{k}{M}p = \delta - 2\,\omega_r\frac{p}{\hbar k} \\ \delta'_{31}(p) &= \delta'_{32}(p) - \delta'_{12}(p)\,. \end{aligned} \qquad (18)$$

In Equation 17, the effect of the vacuum has been taken care of by terms proportional to the excited decay rate Γ. Due to the randomness of the spontaneous emission, $N(q)$ is:

$$N(q) = \frac{3}{8\hbar k}\left[1 + \left(\frac{q}{\hbar k}\right)^2\right], \qquad (19)$$

assuming that the emitted photon is circularly polarized. [2] The increase in the ground state population by this process is represented by the two integrations in Equation 17.

THE STEADY STATE SOLUTION

To obtain the steady state solution, all the time derivatives in Equation 17 are set to zero. This leads to 9 coupled equations:

$$0 = \Gamma\rho_{11}(p,t) - i\left[E\rho_{21}(p,t) - E^*\rho_{12}(p,t)\right] \qquad (20a)$$

$$0 = \Gamma\rho_{33}(p,t) - i\left[E\rho_{23}(p,t) - E^*\rho_{32}(p,t)\right] \qquad (20b)$$

$$0 = \left[0.5\Gamma - i\delta'_{12}(p)\right]\rho_{12}(p,t) - iE\left[\rho_{22}(p,t) - \rho_{11}(p,t)\right] + iE\rho_{13}(p,t) \qquad (20c)$$

$$0 = \left[0.5\Gamma - i\delta'_{32}(p)\right]\rho_{32}(p,t) - iE\left[\rho_{22}(p,t) - \rho_{33}(p,t)\right] + iE\rho_{31}(p,t) \qquad (20d)$$

$$0 = \left[\Gamma - i\,\delta'_{31}(p)\right]\rho_{31}(p,t) - i\left[E\,\rho_{21}(p,t) - E^{*}\,\rho_{32}(p,t)\right] \quad (20e)$$

$$0 = \Gamma\int_{-\hbar k}^{+\hbar k} dq\, N(q)\,\rho_{11}(p+\hbar k+q,t) + \Gamma\int_{-\hbar k}^{+\hbar k} dq\, N(q)\,\rho_{33}(p-\hbar k+q,t) - i\left[E\rho_{21}(p,t) - E^{*}\rho_{12}(p,t)\right] - i\left[E\rho_{23}(p,t) - E^{*}\rho_{32}(p,t)\right] \quad (20f)$$

$$0 = \left[0.5\Gamma + i\delta'_{12}(p)\right]\rho_{12}(p,t) + iE^{*}\left[\rho_{22}(p,t) - \rho_{11}(p,t)\right] - i\,E^{*}\,\rho_{31}(p,t) \quad (20g)$$

$$0 = \left[0.5\Gamma + i\delta'_{32}(p)\right]\rho_{23}(p,t) + iE^{*}\left[\rho_{22}(p,t) - \rho_{33}(p,t)\right] - i\,E^{*}\,\rho_{13}(p,t) \quad (20h)$$

$$0 = \left[\Gamma + i\delta'_{31}(p)\right]\rho_{13}(p,t) + i\left[E^{*}\,\rho_{12}(p,t) - E\,\rho_{23}(p,t)\right] \quad (20i)$$

A method of dealing with coupled equations is to first use a forward substitution to reduce the coupled equations to one equation involving one unknown and then use a backward substitution to obtain all the unknowns in terms of the one equation with one unknown. We begin the substitution process by solving Equations 20*c*, 20*d*, 20*g* and 20*h* for $\rho_{12}(p)$, $\rho_{21}(p)$,$\rho_{32}(p)$ and $\rho_{23}(p)$ in terms of the populations $\rho_{31}(p)$ and $\rho_{13}(p)$. We then substitute these results back into Equations 20*a*, and 20*b*. From this, we find two sources of contributions to the excited populations. The first can be traced to the single-photon process.

The effect of the single photon process on the atomic populations can be represented by the single photon absorption (emission) rates:

$$a_{12}(p) = \frac{\Gamma I}{0.25\,\Gamma^2 + \delta'^{\,2}_{12}}$$
$$a_{21}(p) = \frac{\Gamma I}{0.25\,\Gamma^2 + \delta'^{\,2}_{32}} \quad (21)$$

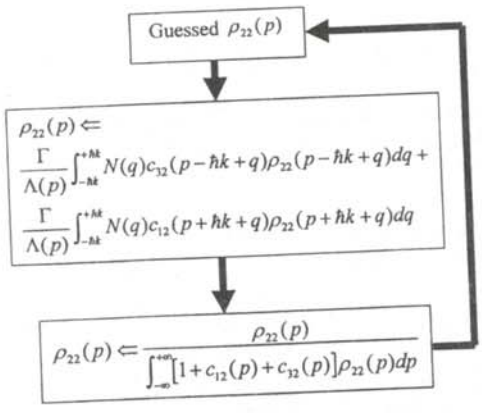

Figure 2

Flow chart of the numerical method used in the self-consistent approach.

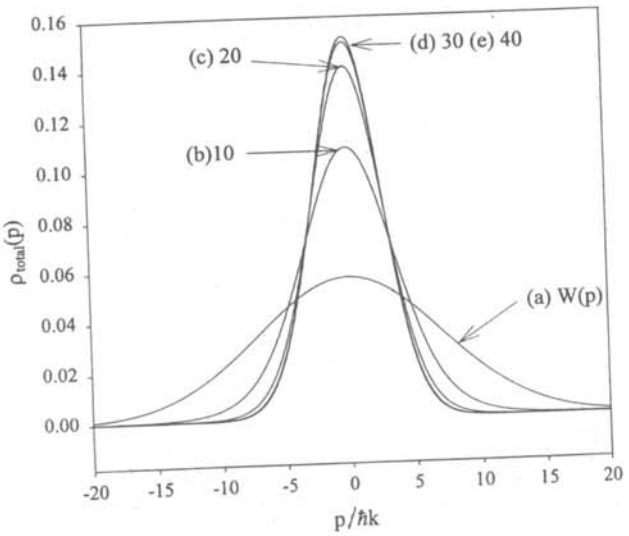

Figure 3

Total momentum distribution, $\rho_{total}(p)$ generated after b) 10, c) 20, d) 30 and e) 40 iterations. The initial guess is a Gaussian function with width $\Delta p_D = 10\hbar k$. Other parameters used in the simulations are: $\omega_r = 0.02657\Gamma$, $E = 0.1\Gamma$ and $\delta = -0.6\Gamma$

where $I = |E|^2$ is the intensity of the laser. The second contribution is due to the excited coherences $\rho_{31}(p)$ and $\rho_{13}(p)$ established by the two-photon process.[6] The two photon process is characterized by the net escaping rate of the atoms at level 1:

$$A_{11}(p) = 2I^2\,\frac{(0.25\,\Gamma_1^{\,2} + \delta'^{\,2}_{12})G_{31} + \Gamma_1\,\delta'_{12}\,S_{31}}{(0.25\,\Gamma_1^{\,2} + \delta'^{\,2}_{12})^2\,(G_{31}^{\,2} + S_{31}^{\,2})}, \quad (22)$$

the net escaping rate of atoms at level 3:

$$A_{33}(p) = 2I^2\,\frac{(0.25\,\Gamma_3^{\,2} + \delta'^{\,2}_{32})G_{31} + \Gamma_3\,\delta'_{32}\,S_{31}}{(0.25\,\Gamma_3^{\,2} + \delta'^{\,2}_{32})^2\,(G_{31}^{\,2} + S_{31}^{\,2})}, \quad (23)$$

and finally the population exchange rate between levels 1 and 3:

$$A(p) = 2I^2\,\frac{(0.25\,\Gamma_1^{\,2} + \delta'_{12}\delta'_{32})G_{31} + \Gamma_3\,(\delta'_{12} - \delta'_{23})\,S_{31}}{(0.25\,\Gamma_1^{\,2} + \delta'^{\,2}_{12})\,(0.25\,\Gamma_3^{\,2} + \delta'^{\,2}_{32})\,(G_{31}^{\,2} + S_{31}^{\,2})}, \quad (24)$$

where:

$$G_{31}(p) = \Gamma_1 + \frac{0.5\,\Gamma_1\,I}{0.25\,\Gamma_1^{\,2} + \delta'^{\,2}_{12}} + \frac{0.5\,\Gamma_3\,I}{0.25\,\Gamma_3^{\,2} + \delta'^{\,2}_{23}}$$
$$S_{31}(p) = \delta'_{31} + \frac{I\,\delta'_{12}}{0.25\,\Gamma_1^{\,2} + \delta'^{\,2}_{12}} - \frac{I\,\delta'_{32}}{0.25\,\Gamma_3^{\,2} + \delta'^{\,2}_{23}}. \quad (25)$$

These rates are deduced by expressing $\rho_{31}(p)$ and $\rho_{13}(p)$ in terms of the population terms with the help of Equations 20*c*, 20*d*, 20*e*, 20*g*, 20*h* and 20*i*. These steps reduce Equations 20*a* and 20*b* into steady state rate equations from which the excited state populations, $\rho_{11}(p)$ and $\rho_{33}(p)$ can be written in terms of the ground state population, $\rho_{22}(p)$ as:

$$\rho_{11}(p) = c_{12}(p)\,\rho_{22}(p)$$
$$\rho_{33}(p) = c_{32}(p)\,\rho_{22}(p)\,. \qquad (26)$$

where

$$c_{12}(p) = \frac{R_{12}(\Gamma_3 + R_{32}) - A\,[\Gamma_3 + A]}{(\Gamma_1 + R_{12})\,(\Gamma_3 + R_{32}) - A^2}$$
$$c_{32}(p) = \frac{R_{32}(\Gamma_1 + R_{12}) - A\,[\Gamma_1 + A]}{(\Gamma_1 + R_{12})\,(\Gamma_3 + R_{32}) - A^2}\,, \qquad (27)$$

and

$$R_{12}(p) = a_{12}(p) - A_{11}(p)$$
$$R_{32}(p) = a_{32}(p) - A_{33}(p) \qquad (28)$$

Finally, we combine Equations 20*a*, 20*b* and 20*f* and transform the results with the help of Equation 26 into an integral equation the single unknown function, $\rho_{22}(p)$:

$$\rho_{22}(p) = \frac{\Gamma}{\Lambda(p)}\int_{-\hbar k}^{+\hbar k} dq\, N(q)\, c_{32}(p - \hbar k + q)\,\rho_{22}(p - \hbar k + q)$$
$$+ \frac{\Gamma}{\Lambda(p)}\int_{-\hbar k}^{+\hbar k} dq\, N(q)\, c_{12}(p + \hbar k + q)\,\rho_{22}(p + \hbar k + q), \qquad (29)$$

where

$$\Lambda(p) = \Gamma_1\, c_{12}(p) + \Gamma_3\, c_{32}(p)\,. \qquad (30)$$

In addition, $\rho_{22}(p)$ is constrained by the normalization condition:

$$\int_{-\infty}^{+\infty}\left[\rho_{11}(p) + \rho_{22}(p) + \rho_{33}(p)\right] dp = 1\,, \qquad (31)$$

which can be written using Equation 20 as:

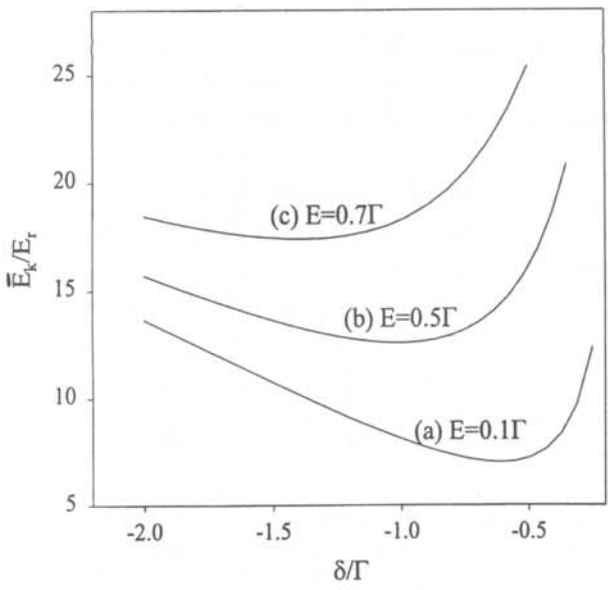

Figure 4

The average kinetic energy vs laser detuning for a) E = 0.1Γ, b) E = 0.5Γ and c) E = 0.5Γ. ω_r for these curves is 0.02657Γ

$$\int_{-\infty}^{+\infty}\left[1 + c_{12}(p) + c_{3c}(p)\right]\rho_{22}(p)\,dp = 1\,. \qquad (32)$$

NUMERICAL SIMULATION AND DISCUSSION

The key determining the steady-state atomic distribution is the solution of the integral Equation 29. Once $\rho_{22}(p)$ is determined, the momentum distributions in the excited states can be obtained using Equations 26. We take advantage of the normalization condition in Equation 32 and propose a method based on the concept of self-consistency to solve Equation 29.

The self-consistent loop is illustrated in Figure 2. A distribution function is guessed for $\rho_{22}(p)$. With the guessed value for $\rho_{22}(p)$, the right side of Equation 29 is evaluated explicitly to yield a new momentum distribution for the ground state. This newly produced $\rho_{22}(p)$, after a normalization according to Equation 32, assumes the role of the guessed one and the process is repeated. When the shape of the function $\rho_{22}(p)$ does not change with further iterations, the state of self-consistency is reached and the unchanged $\rho_{22}(p)$ is the desired steady state solution. If we do not reach a shape for $\rho_{22}(p)$ that does not change, the steady state solution does not exist.

In our simulation, the unit of momentum is chosen to be $\hbar k$ and Γ is the unit for any rates and frequencies. The guessed value for $\rho_{22}(p)$ is assumed to be a normalized Gaussian function:

$$\rho_{22}(p) = \frac{1}{\sqrt{2\pi}\,\Delta p_D}\, e^{-\left(\frac{p}{\Delta p_D}\right)^2}, \qquad (33)$$

where Δp_D is the half width of the distribution. The momentum is sampled at a rate between 10 and 20 divisions per $\hbar k$. In the simulation, we calculate the total momentum distribution, defined as:

$$\rho_{total}(p) = c_1(p)\,c_1^*(p) + c_2(p)\,c_2^*(p) + c_3(p)\,c_3^*(p)\,. \qquad (34)$$

Using Equation 16, Equation 34 can be written as:

$$\rho_{total}(p) = \rho_{11}(p + \hbar k) + \rho_{22}(p) + \rho_{33}(p - \hbar k) \qquad (35)$$

We also calculate the average kinetic energy:

$$\bar{E}_k = \langle\psi|\frac{\hat{p}^2}{2M}|\psi\rangle = \int_{-\infty}^{+\infty}\frac{p^2}{2M}\,\rho_{total}(p)\,dp\,, \qquad (36)$$

which is a direct measure of the temperature of the atomic ensemble. The integrations are all done using Simpson's rule. [7]

We first consider the λ = 1.083 μm transition in ^{4}He atoms for which $\omega_r = 0.02657\Gamma$. Figure 3 shows several results for low intensity $E = 0.1\Gamma$ and $\delta = -0.6\Gamma$. We start with the guessed $\rho_{22}(p)$ with $\Delta p_D = 10\hbar k$ (curve *a*) and then did 10 iterations (curve *b*), 20 iterations (curve *c*), 30 iterations (curve *d*) and 40 iterations (curve *e*). The difference between the results for 30 iterations and 40 iterations is extremely small, so we conclude that the state of self-consistency is reached in about 40 iterations. The width of the momentum distribution is $3\hbar k$, and the average kinetic

energy is 7.04 E_r.

Figure 4 shows how the average kinetic energy changes with the laser detuning δ for different values of E. The average kinetic energy reaches a minimum, $\bar{E}_{k\,min}$, at laser detuning δ_{min}. Note that both $|\delta_{min}|$ and $\bar{E}_{k\,min}$ increase with the Rabi frequency.

The existence of an optimal detuning at which the kinetic energy is minimum (meaning the lowest temperature) is a manifestation of laser cooling. If the detuning is too far below the atomic transition, the net force resulting from the Doppler shift between the counter and copropagating laser fields is relatively weak, so the cooling efficiency is not high, If, on the other hand, the detuning is too close to the atomic transition, atoms of even moderate velocities "see" the frequencies of both lasers to be larger than the atomic transition frequency, so the counter propagating laser is further away in energy from the atomic transitions than the copropagating one. The net effect is that the motion of these atoms, instead of being slowed down, is accelerated, leading to heating of the atoms.

In fact, we found that if δ is some frequency above δ_{min}, the momentum distribution keeps expanding as the number of iterations increases. Physically this means that momentum diffusion due to the spontaneous emission overcomes the radiation cooling, so a steady state distribution cannot be reached.

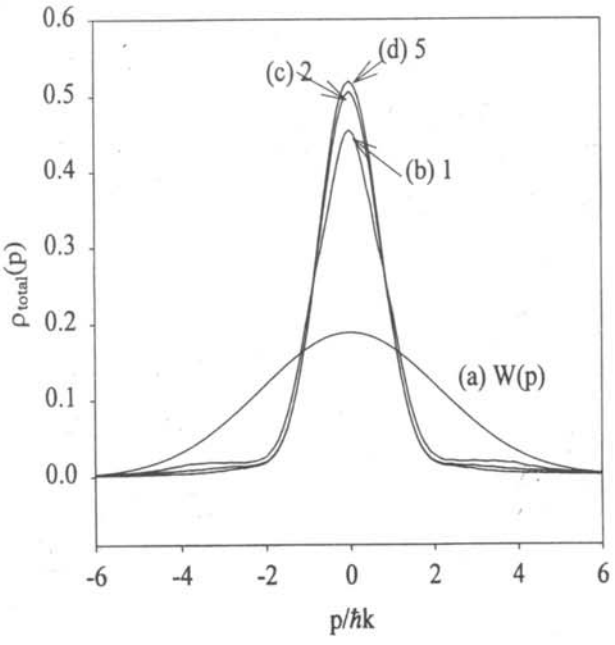

Figure 5

Total momentum distribution, $\rho_{total}(p)$ generated after b) 1, c) 2, d) 5 iterations. The initial guess is a Gaussian function with width $\Delta p_D = 3\hbar k$. Other parameters used in the simulations are: ω_r=10Γ, E = 10Γ and δ = -38Γ.

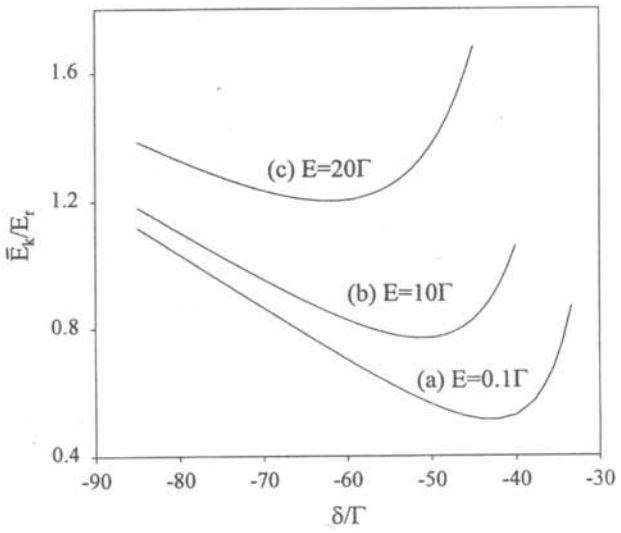

Figure 6

The average kinetic energy vs laser detuning for a) E = 0.1Γ, b) E = 10Γ and c) E = 20Γ. ω_r for these curves is 10Γ.

We worked out a case where the recoil shift was much larger than the excited decay rate: ω_r = 10Γ, E = 10Γ and δ = -38Γ. We began with an initial Gaussian function with $\Delta p_D = 3\hbar k$. Figure 5 shows the results. Curve *a* is the initial shape of $\rho_{22}(p)$. Curve *b* is after 1 iteration, curve *c* after 2 iterations and curve *d* is after 5 iterations. Remarkably, the state of self-consistency is reached after only several iterations. The width of the momentum after these iterations is about $0.9\hbar k$, much narrower than that shown in Figure 3. As ω_r/Γ increases, the momentum distribution narrows. The average kinetic energy was 1.43 E_r.

In both of the cases discussed, the momentum width is on the order of the single photon momentum. As a result, a momentum change of $\hbar k$ is not negligible. The full quantum mechanical treatment of the atomic variables is justified.

The change in the average kinetic energy vs the laser detuning is displayed in Figure 6 for different Rabi frequencies. Again, it shows that there exists an optimal laser detuning at which the average kinetic energy, or equivalently the temperature of the atoms, is a minimum.

Previous theoretical work [2] predicted that for narrow momentum distributions (large ω_r/Γ) in the low intensity limit (small E/Γ), $\delta_{min} \approx -4.5\omega_r$ and $\bar{E}_{k\,min} \approx 0.530\ \hbar\ \omega_r$. The curve in Figure 6 is produced with parameters close to these limits (ω_r/Γ=10>>1 and E/Γ = 0.1 << 1). The minimum kinetic energy is reached at $\delta_{min} \approx -43.1\Gamma = -4.31\omega_r$ with $\bar{E}_{k\,min} \approx 0.513\ \hbar\ \omega_r$. These results are indeed quite close to the theoretical predictions.

ACKNOWLEDGMENTS

This work was supported by a grant from the Research Corporation. The author wishes to thank Dr. Hong. Y.

Ling for his advice and support.

REFERENCES

* current address of author: Anthony Williams, Department of Physics, University of Notre Dame, Notre Dame, IN 46556. Williams.237@nd.edu

1. For a tutorial on laser cooling, see for example, Laser Cooling and Trapping of Atoms, Special issue edited by S. Chu and C. Wieman, J. Opt. Soc. Am., B 6 (1989).
2. Y. Castin, H. Wallis and J. Dalibard, "Limit of Doppler Cooling", J. Opt. Soc. Am., B 6. (1989) p. 2046.
3. D.J. Griffiths, Introduction to Quantum Mechanics, Prentice Hall, (1994).
4. D. Halliday, R. Resnick and J. Walker, Fundamentals of Physics, 5th Ed., John Wiley, (1997).
5. L. Allen and J.H. Eberly, Optical Resonance and Two-Level Atoms, John Wile, (1975).
6. H.Y. Ling, "Several Asymptotic Subrecoil Laser-Cooling Behaviors in Arbitrary Degenerate Λ Systems", Phys. Rev. A59, (1999), p. 3714.
7. W.H. Press, Flannery, S.A. Teukolsky and W.T. Vetterling, Numerical Recipes in C, Cambridge, (1998).

FACULTY SPONSOR

Dr. Hong Y. Ling
Department of Chemistry and Physics
Rowan University
Glassboro, NJ 08028
ling@elvis.rowan.edu

DETERMINATION OF THE TEMPERATURE DEPENDENCE OF YOUNG'S MODULUS FOR STAINLESS STEEL USING A TUNING FORK

Lisa Bates*, Timothy Beach# and Maya Arnott†
Physics Department
University of Wisconsin - River Falls
River Falls, WI 54022
received June 7, 1999

ABSTRACT

Tuning forks have been used as high quality frequency standards for decades. Musicians are well aware of the effect that temperature has on the tuning of their instruments. Those effects are generally attributed to either a change in the speed of sound in air (for wind instruments) or thermal expansion for string and percussion instruments. We show that in the case of a tuning fork, thermal expansion is a minor consideration. The primary source of the temperature dependence of the tuning fork is caused by a temperature dependence in the Young's modulus of the material out of which it is made. The stiffness of the fork changes slightly with temperature, causing a change in the resonant frequency of the tuning fork. We use this effect to determine an empirical formula for the temperature dependence of stainless steel.

INTRODUCTION

The first person to tune musical instruments with a tuning fork was Pythagoras in the sixth century BC. It is believed that he created the diatonic musical scale. [1] Most applications of tuning forks use the fork as a frequency reference standard. Musicians usually tap a tuning fork to get a fixed pitch, against which they tune their instruments.

At one time, physicists used tuning forks as frequency standards. Now, the physics of tuning forks is interesting in other ways. Research is done on the modes of vibration or the nonlinear motion of the tines. [2] The literature, however, does not have much to say about the temperature dependence of tuning forks. [3,4]

Lisa is a physics and mathematics double major and has a minor in chemistry. She graduates from the University of Wisconsin - River Falls in December of 1999. After graduation, she plans to pursue employment in industry.

Tim is a senior majoring in physics and minoring in mathematics. He plans to graduate in the spring of 2000. In his spare time, Tim enjoys competitive swimming and chasing storms.

Maya is a senior with a double major in physics and mathematics. She plans to go to graduate school in astrophysics. She enjoys spending time outside, running and listening to music.

Musical instruments have pitches that vary with temperature. The variation of pitch for percussion and string instruments is generally attributed to the thermal expansion of the instrument. For wind instruments, variations in the velocity of sound in air cause the frequency variation. The variation in pitch is very noticeable in wind instruments of the flute type. Consequently, wind instruments must be 'warmed up' before tuning; the player's breath will determine the actual temperature within the instruments. Before air conditioning for auditoriums, orchestras would adjust the pitch of their instruments to match the piano, because the pitch of the piano does not have much temperature dependence. Even so, the piano itself must be tuned at some temperature.

In the mid 19th century, there was a discussion about the appropriate reference temperature at which an instrument was tuned. In 1859, the French Commission chose 50 F as the standard pitch temperature. Later on, the British Standard Institution recommended 20 C or 68 F. The standard pitch and its associated temperature for instruments today is 440 Hz at 20 C. [5]

Literature in the area of tuning fork acoustic behavior is somewhat limited. Lord Rayleigh did some research concerning tuning forks; he observed that small masses

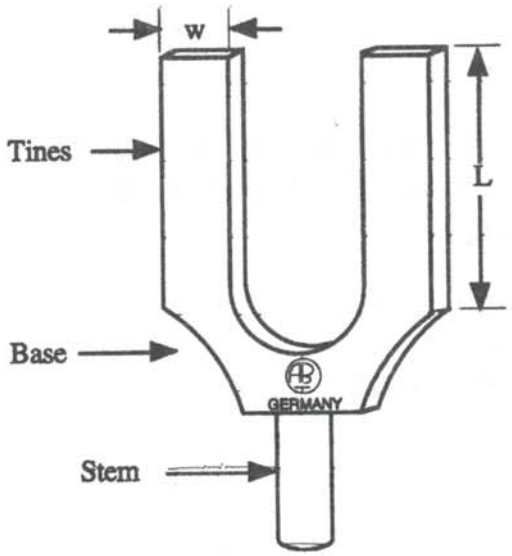

Figure 1
Schematic diagram of the tuning fork showing the relevant dimensions. The trademark etched on the base was not identified in any of our database searches.

hanging from the tines decreased fundamental stem motion. [6] Surprisingly little information on the temperature dependence of the tuning fork resonance frequency can be found. A previous experiment done by University of Wisconsin - River Falls students found that the resonant frequency decreased as a linear function of temperature in the temperature range between 24 C and 30 C. [7]

Thermal expansion, which is generally cited as the cause of the shift in frequency for percussion and string instruments, cannot account for the shift of the resonant frequency. The temperature dependence of Young's modulus has been demonstrated to be the dominant effect in determining the temperature dependence of the resonant frequency of small tuning forks made of materials such as crystalline silicon and zirconium. [8] In this paper, we extend this research to show how the temperature dependence of Young's modulus affects ordinary tuning forks.

THEORY

A simple tuning fork, such as the one shown in Figure 1, can be thought of as two straight bars, each of which is clamped at one end. From an examination of how the bars bend when they vibrate, the resonant frequency, f_n, can be shown to be: [8]

$$f_n = \frac{\pi}{16\sqrt{3}} \frac{w}{L^2} \sqrt{\frac{E}{\rho}}\, c_n, \qquad (1)$$

where w and L are the width and length of the tuning fork tines; E is Young's modulus; ρ the density of the material; n, is the mode number, an integer greater than 0; and c_n is a multiplication factor that depends on the mode. c_n is represented by the sequence:

$$c_n = (1.194)^2, (2.988)^2, (5)^2, \ldots, (2n-1)^2 \quad n > 2. \qquad (2)$$

The temperature dependence of the expansion of the bars can be modeled as:

$$w(T) = w_o \left[1 + \int_{T_o}^{T} \alpha_l(T)\, dT\right]$$
$$L(T) = L_o \left[1 + \int_{T_o}^{T} \alpha_l(T)\, dT\right] \qquad (3)$$
$$\rho(T) = \frac{\rho_o}{\left[1 + \int_{T_o}^{T} \alpha_v(T)\, dT\right]},$$

where w_o, L_o and ρ_o are the dimensions and density at temperature T_o, α_l is the linear coefficient of thermal expansion, and $\alpha_v \approx 3\alpha_l$ is the volume coefficient of thermal expansion.

In the small temperature range of this experiment, the coefficients of thermal expansion are approximately constant, so Equations 3 can be written as:

$$w(T) = w_o \left[1 + \alpha_l(T - T_o)\right]$$
$$L(T) = L_o \left[1 + \alpha_l(T - T_o)\right] \qquad (4)$$
$$\rho(T) = \frac{\rho_o}{\left[1 + \alpha_v(T - T_o)\right]}.$$

When Equation 4 is inserted into Equation 1, the temperature dependence of the frequency, $f_n(T)$, becomes:

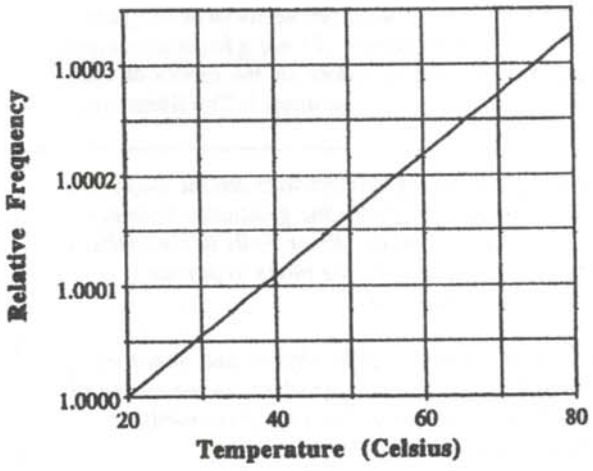

Figure 2
A numerical prediction of the effects of thermal expansion on the resonant frequency, ignoring any possible temperature dependence of Young's modulus. Note the very modest increase in frequency.

$$\frac{f_n(T)}{f_{n,o}} = \frac{\sqrt{\left[1 + \alpha_v(T - T_o)\right]}}{\left[1 + \alpha_l(T - T_o)\right]}, \qquad (5)$$

where $f_{n,o}$ is the frequency at temperature T_o. Figure 2 is a plot of the relative frequency over a temperature range used in this experiment for our tuning forks. The slope of the line is positive, with a value of 5 parts/million/C which is essentially zero. The actual behavior of the tuning fork shows a decrease in frequency of 1 percent as the temperature increases in this range. Hence a simple thermal expansion model does not predict the correct temperature dependence.

In the derivation of Equation 5, we assumed that Young's modulus is independent of temperature. Including a possible temperature dependence for Young's modulus gives:

$$\frac{f_n(T)}{f_{n,o}} = \frac{\sqrt{\left[1 + \alpha_v(T - T_o)\right]}}{\left[1 + \alpha_l(T - T_o)\right]} \sqrt{\frac{E(T)}{E_o}}, \qquad (6)$$

where $E(T)$ is Young's modulus at temperature T and E_o is Young's modulus at temperature T_o. The results shown in Figure 2 imply that we can ignore the thermal expansion terms. Rewriting Equation 6 gives:

$$\frac{E(T)}{E_o} = \left(\frac{f_n(T)}{f_{n,o}}\right)^2 \frac{\left[1 + \alpha_l(T - T_o)\right]^2}{\left[1 + \alpha_v(T - T_o)\right]}. \qquad (7)$$

We use Equation 7 to transform our values of relative frequency into relative Young's modulus.

THE EXPERIMENT

Alloy determination

The tuning fork we used was made of an unknown composition steel. A search of physics catalogs and a computerized trademark (see Figure 1) search of registered companies as well as discussions with the music department were fruitless in determining the composition of the steel used in the manufacture of the forks. So, we decided to determine the particular stainless steel by determining its density.

To determine the density of the tuning fork, we employed a technique used by geologists to find the density of irregular objects known as a Jolly balance. We measured the weight of the tuning fork in air, W_{air}, and in distilled water, W_{water}. The density is found as:

$$\rho = \rho_{water} \frac{W_{air} - W_{water}}{W_{air}} = 7.767 \pm 0.006\, g/cm^3. \qquad (8)$$

where $\rho_{water} = 0.998203$ g/cm^3. We compared this result with density information on various types of stainless steel. [10] We concluded that the tuning fork was most probably formed from a cutlery stainless steel. The cutlery stainless steel included 0.2% to 0.4% C, 0.2% Si, 0.35%Mn and 12% to 15% Cr; the remaining content is Fe.

Temperature determination

The temperature of the tuning fork was determined by an oven controlled by a variable auto transformer. Thermistors [11] were used to monitor the temperature. One was placed on a dab of glycerin on the metal plate clamping the tuning fork in place. A second thermistor was suspended in the air of the oven to measure the air temperature. The calibration data supplied by the manufacturer were fit to an appropriate series and used to convert the thermistor resistance, measured by a multimeter [12], in kΩ into temperature values in C. The uncertainty in our temperature values was ±0.1 C.

We monitored both the air temperature and the tuning fork temperature to avoid thermal lag. We found that the best way to minimize the thermal lag was to heat the oven and to regulate its rate of cooling by gradually decreasing the voltage supply. Using this technique, the two temperatures remained within 2 C of each other.

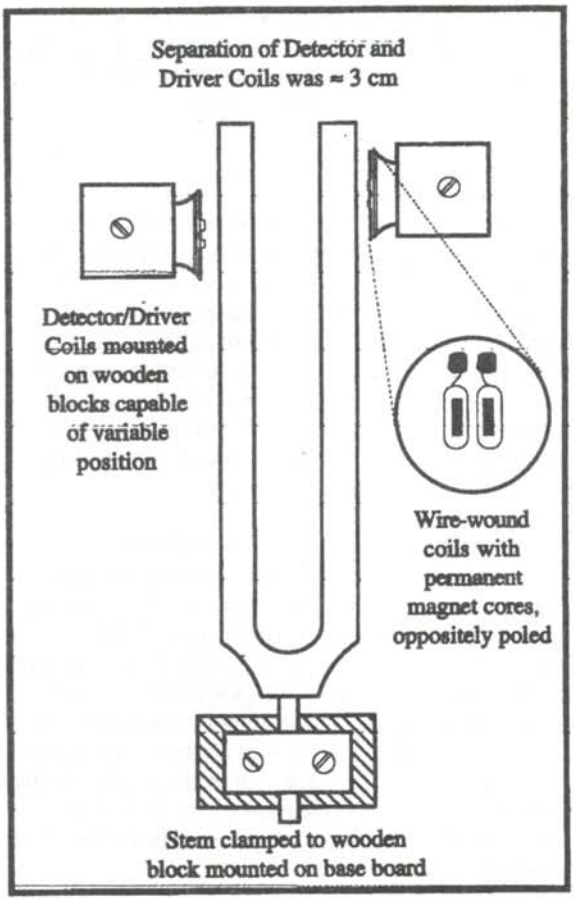

Figure 3

Schematic diagram of the apparatus. All components were mounted on a wooden base such that the relative positions of the coils and the tuning fork could be controlled. The inset shows an end-on view of one of the driver/detector coils.

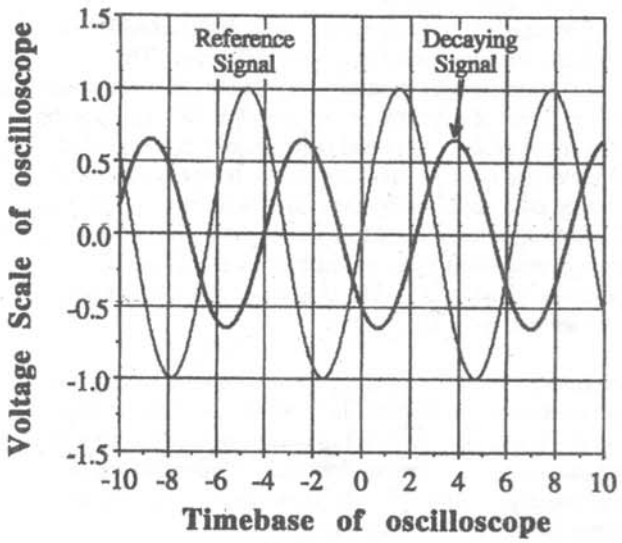

Figure 4

Representation of the oscilloscope trace. The signal generator provided a stable reference signal. As the signal from the tuning fork decays, any mismatch in frequency will result in a lateral shift of the decaying signal.

Driving the tuning fork

We used electromagnets salvaged from a pair of old earphones to drive and record the motion of the tuning fork tines. Each earphone contained two antiparallel coils, each wrapped around a permanent magnet core. The mounting system and coils are shown in Figure 3. The earphones were mounted so that the polarities of the driver coils were opposite to the polarities of the detector coils. The earphones could be clamped in various locations relative to the tuning fork to allow us to tune the response of the system for optimal performance.

When an alternating current is sent through the driver coil, the oscillating electromagnetic field interacts with the ferromagnetic material in the tuning fork. The resulting vibration of the tines in the electromagnetic field of the detector coil produces eddy currents, which in turn induce current in the detector coil. This system, unfortunately, was very sensitive to background electromagnetic noise. We had to turn off all the fluorescent lights in the lab to minimize the detection of noise. In principle, this system could be used to drive and measure the motion of an aluminum tuning fork, but the response was too small for us to measure.

Measuring the resonant frequency

Given the leisurely pace of this experiment (to avoid thermal lag), we felt free to use a leisurely method of measuring the resonant frequency. We used a variation on the Lissajous figure technique where one channel of an *x*-*y* oscilloscope is fed a reference frequency and the other channel is fed the signal. If the figure drawn on the face of the oscilloscope is an ellipse that seems to rotate, the two frequencies do not match. The reference frequency then is adjusted to freeze the Lissajous pattern, indicating that the two frequencies are the same. However, the decay of the signal input from the damped tuning fork presents the illusion of rotation in the Lissajous figure, even when the two frequencies are identical. Thus, we had to modify the technique and adapted one usually used for measuring relative phase between two signals. [13]

The oscilloscope is set into a time base mode and the reference signal is used as the time trigger for the sweep. This eliminates effects of a changing reference signal. Figure 4 is a sketch of the oscilloscope face showing the reference signal and the decaying signal produced by the damped tuning fork. The tuning fork initially is set into oscillation by connecting the driver coil to the reference signal. The frequency of the reference signal is set close to the resonant frequency of the tuning fork. The tuning fork quickly builds up a large amplitude of oscillation. The driver coil is then disconnected from the reference signal and the tuning fork allowed to freely oscillate at its natural resonant frequency. If the resonant frequency does not exactly match the reference frequency, the two signals will steadily accumulate a phase shift with respect to each other. This is seen on the oscilloscope face by a drift in the displayed signal from the pick-up coils near the oscillating tuning fork. The frequency of the reference is adjusted to 'freeze' the horizontal drift of the signal from the tuning fork. When the oscilloscope trace is 'frozen', the two frequencies are the same. The limit of the precision of this technique is governed by the precision of the frequency generator [14] and the amount of time that the decaying signal can be monitored before it disappears into the noise. We were able to track the resonant frequency of about 128 Hz as a function of temperature to ±0.003 Hz.

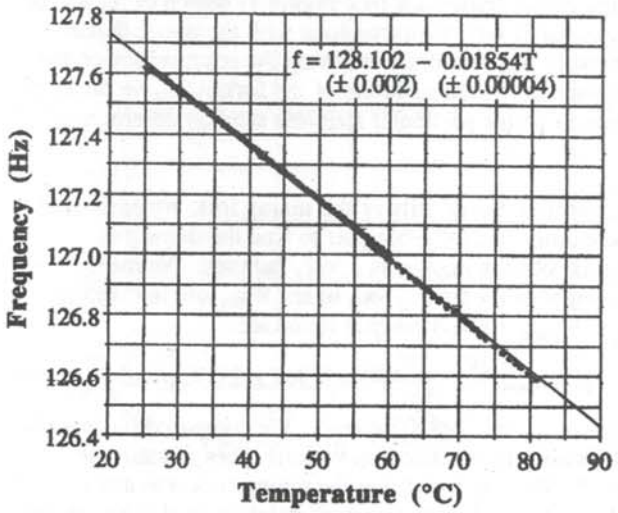

Figure 5

Results of frequency measurements in the temperature range 25 C to 80 C. The graph shows an almost linear dependence with a negative slope.

EXPERIMENTAL RESULTS

Figure 5 shows our measurements of the resonant frequency of the tuning fork as a function of temperature. The frequency vs temperature graph appears almost linear with a slope of -0.01854±0.00004 Hz/C.

The data shown in Figure 5 are transformed into a graph of the relative dependence of Young's modulus using Equation 7. The reference frequency, $f_{\vec{n},\vec{o}}$, was picked as the frequency at 'room temperature' of 18.88 C (a rather chilly lab); 127.727±0.003 Hz. We ignore all thermal expansion factors. Figure 6 shows the measured relative values of Young's modulus as a function of temperature. The temperature dependence is best fit by a quadratic function:

$$\frac{E(T)}{E_o} = (1.00501 \pm 0.00005) - (2.55 \pm 0.02)\times 10^{-6} C^{-1}\, T - (4.5 \pm 0.2)\times 10^{-8} C^{-2}\, T^2, \quad (9)$$

which is consistent with the nearly linear behavior of the frequency vs temperature graph shown in Figure 5. These results show that Young's modulus for stainless steel has a quadratic dependence on temperature between 20 C and 80 C.

ACKNOWLEDGMENTS

The authors would like to thank Dr. Earl Blodgett for his assistance throughout this project. His support was essential to its completion

REFERENCES

* current address of author: PO Box 311, Spring Valley, WI 54767.

\# current address of author: 134 McMillan Hall, 706 East Cascade Avenue, River Falls, WI 54022.

† current address of author: 950 south Main Street, #2B, River Falls, WI 54022.

1. J. Dumm, http://t-hyp.com/products/tuningforksmore.html., 1999.
2. T. Rossing, et. al, "On the Acoustics of Tuning Forks", Am. J. Phys., 60, (July 1992), pp. 620-626.
3. D.W. Schindel, D.A. Hutchins and D.T. Smith, J. Acoust. Soc. Am., 102, (1997), pp. 1296-1308.
4. D.W. Schindel, private communication.
5. A. Wood, The Physics of Music, 6th ed, Methuen & Co., Ltd., (1962), pp. 49-50.
6. J. Woo, http://home.hkstar.com/~joewoo/rayleigh.html, July 1998.
7. J. Kalk, M. Jorgenson, B. Zadler, private communication.
8. P. Morse and K. Ingard, Theoretical Acoustics, McGraw-Hill, (1968).
9. CRC-Handbook of Chemistry and Physics, 46th ed., Chemical Rubber Co., (1964), p. F-4.
10. Metals Handbook, American Society for Metals, (1939), p. 537.
11. PASCO TD-8559 Thermistor Probe, PASCO Scientific, PO Box 619011, 10101 Foothills Boulevard, Roseville, CA 95661-9011.
12. HP 34401A Multimeter, Hewlett Packard Corp., 3000 Hanover Street, Palo alto, CA 94304.
13. User Manual - 2212 Digital Storage & Analog Oscilloscopes, Tektronix, Inc., Beaverton, OR, (1992), pp. 3-18.
14. DS340 15 MHz Synthesized Function Generator, Stanford Research Systems, 1290-D Reamwood Avenue, Sunnyvale, CA 94089.

FACULTY SPONSOR

Dr. Earl Blodgett
Department of Physics
University of Wisconsin- River Falls
River Falls, WI 54022
earl.d.blodgett@uwrf.edu

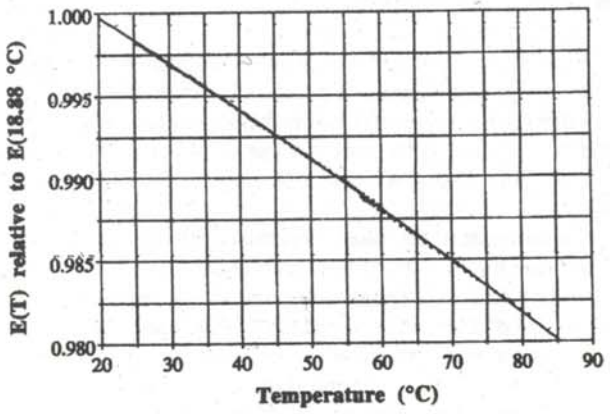

Figure 6
Temperature dependence of Young's modulus expressed as a ratio relative to the value at 18.88 C.

PHONON MODES IN InAs/AlSb SUPERLATTICES

Josh Matsko *
Department of Physics
Illinois State University
Normal, IL 61761
received January 12, 2000

ABSTRACT

The InAs/AlSb heterojunction system is a lattice matched semiconductor system with type-II band alignment at the interfaces. This system is attractive to ultra-fast electronic device application due to its high mobility and large conduction-band offset. The superlattice can have two different interfaces: AlAs-like or InSb-like. These interfaces have very different interface roughness, mobility and carrier concentrations. There is experimental evidence showing preferential local arrangements of the interfacial atoms. First principle pseudo-potential calculations indicate that such superlattices with switched layers at the interfaces are more energetically favorable than superlattices with ideal sharp strained interfaces. We theoretically calculate the phonon modes of the InAs/AlSb superlattices using a one-dimensional linear chain model. We compare the interface modes for superlattices with the two different interface structures. We found that there not only are more interface modes in the superlattice with the switched interface layers, but that there also exist bulk modes at the interface, a special feature of this structure.

INTRODUCTION

The InAs/AlSb heterojunction system is a lattice matched semiconductor system with type-II band alignment at the interfaces. [1-3] Depending on the structure of an InAs/AlSb superlattice, two types of interfaces can make up the system: AlAs-like or InSb-like. For instance, in Figure 1, an AlAs-like interface is formed. In a one dimensional linear chain model, the interface is named by the 'adjoining' atoms between the two lattices that make up the superlattice. These interfaces have very different interface roughness, mobility and carrier concentrations.

There is experimental evidence showing a preferential local arrangement of the interfacial atoms. [1,2] First principle pseudopotential calculations indicate that such superlattices with switch layers at interfaces are more energetically favorable than superlattices with ideal sharp strained interfaces. [3]

There are four possible types of switches of atomic layers at the interfaces for In As/AlSb superlattices:
1) the anions around Al
2) the anions around In
3) the cations around Sb
4) the cations around As.

It has been shown that the switch of the cations around an anion is energetically more energetically favorable than non-switched interfaces and when the anions are switched around the cations.[3] In our case, the most favorable switch is that of In and Al around As.

To better understand the characteristics of these superlattices, we theoretically calculated the phonon modes, the vibrational frequencies and vibrational amplitudes. Some of these vibrational amplitudes at certain frequencies are more localized at the interface. They are called interface modes. The interface modes are used as variables to model the behavior of the interface.

THE MODEL

We calculate the phonon modes, including the vibrational

Josh has completed the third year of a five-year program that consists of attending Illinois State University (ISU) for the first three years and then the University of Illinois at Urbana-Champaign (UIUC) for two years. After the five years, he will receive a bachelor's degree in physics from ISU and one in mechanical engineering from UIUC. He also has completed the requirements for a math minor at ISU.

This research was started in December of 1998 and there are plans to continue it. The initial results were presented at the Centennial APS meeting in Atlanta in the spring of 1999. During the summer of 1999 he received a REU award from the NSF and traveled to China for three weeks where he continued this research at the Institute of Semiconductors of the Chinese Academy of Sciences.

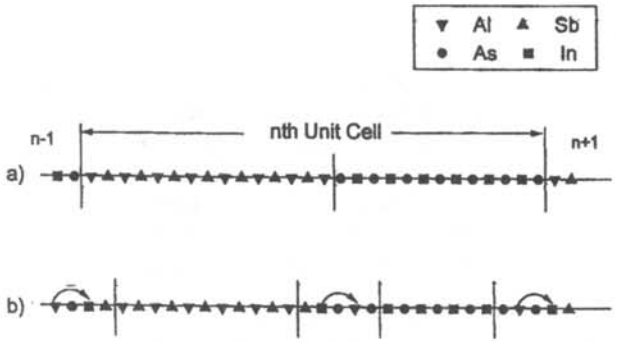

Figure 1
A three-dimensional InAs/AlSb (100) superlattice mapped into a one-dimensional linear chair. (a) the n^{th} unit cell of the superlattice with ideal AlAs-like interfaces. (b) The superlattice with switched layers of In and Al around As at both AlAs-like interfaces

frequencies and vibrations strengths, of the InAs/AlSb superlattice with both the ideal sharp interfaces and with switches of atomic layers at the interfaces. To do this, we used a one-dimensional linear chain model. [4] The three-dimensional InAs/AlSb(100) superlattice was mapped into a one-dimensional linear chain as shown in Figure 1. [5,6] In Figure 1, each atom represents an atomic plane that has the same atoms as in the real superlattice structure. Since all the atoms on the same plane have the same motion when the wave vector is along the superlattice growth direction, one atom can be used to represent the entire atomic plane. In Figure 1, the reversed triangle represents an Al layer, the triangle an Sb layer, the circle an As layer and the square an In layer.

Following the lead of a similar study[5], we considered twenty-eight atomic layers in the unit cell of our superlattice.

The structure of InAs/AlSb (13,15) superlattice with AlAs ideal interfaces is shown in Figure 1a. The structure of the same superlattice, but with cation layers switches around the As layer at the interfaces is shown in Figure 1b. The vertical lines in this figure show where each interface or interface boundary is located.

Our calculations are performed in a manner similar to a previous study [5] of phonon modes in InAs/GaSb superlattices, which uses one force constant for the longitudinal modes and two for the transverse modes and considers only the nearest neightbor interactions. Since the constituent materials of InAs/AlSb superlattices are similar to those of InAs/GaSb superlattices, we used the same force constants: 0.8 N/cm for longitudinal modes and 1.25 N/cm and 0.12 N/cm for the transverse modes. [5]

CALCULATIONS

The calculations start using the Newton's second law of motion. For the ith atom in the nth unit cell, we have:

$$F_i = \sum_{j \neq i} F_{j} = m_i a_i = m_i \frac{d^2 U_{n,i}}{dt^2} \quad , \qquad (1)$$

where F_i is the net force on atom i, $F_{j,i}$ is the force from atom j on atom i, m_i is the mass of atom i, and $U_{n,i}$ is the displacement of the i^{th} atom in the n^{th} unit cell. In Equation 1, l goes from 1 to 28, the total number of atomic layers in the superlattice unit cell.

We assume that each atom acts as a harmonic oscillator, so its displacement can be written as:

$$U_{n,i} = A_{0,i}\, e^{i(kna' - \omega t)} , \qquad (2)$$

where $A_{0,i}$ is the amplitude of the vibration of the i^{th} atom, k is the wave vector, n is the unit cell number, a' is the total length of the unit cell (in our case $28a$ where a is the nearest layer distance), ω is the vibrational frequency and t is time.

To find the net force acting on the ith atom, we consider only the nearest neighbor interaction:

$$F_i = \sum_{j \neq i} F_{j} = F_{i-1} + F_{i+1} \ . \qquad (3)$$

Equation 3 can be put in terms of displacements by recalling that the harmonic oscillator force depends linearly on displacement:

$$F_i = f_i(U_{n,i+1} - U_{n,i}) + f_i(U_{n,i+1} - U_{n,i}) , \qquad (4)$$

where f_i is the force constant between atom i and atom i+1. For the longitudinal modes, all of the force constants are taken to have the same value. For the transverse modes, we have two different force constants.

Substituting Equation 4 into Equation 1 gives:

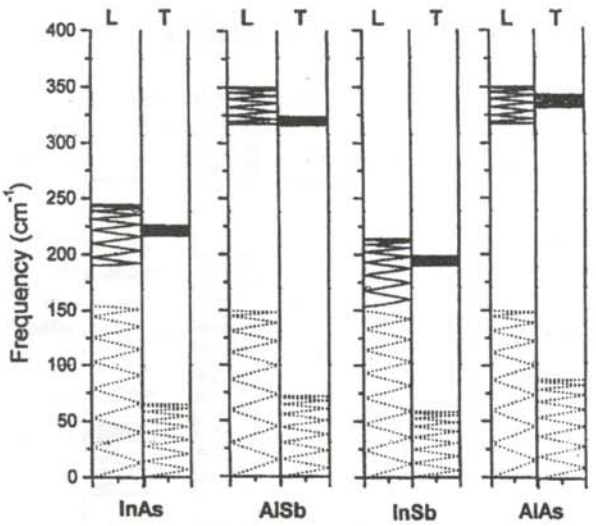

Figure 2
Calculated phonon modes of the four bulk materials: (a) InAs; (b) AlSb; (c) InSb; AlAs. The left panels are for longitudinal (L) modes and the right panels are the transverse (T) modes. The acoustic modes are shown as dotted lines and the optical modes are shown as solid lines.

$$m_i \frac{d^2 U_{n,i}}{dt^2} = f U_{n,i+1} + f_1 U_{n,i-1} - (f + f_1) U_{n,i} . \quad (5)$$

When $i = 1$, the first atom in the unit cell, we consider its interaction with the last atom in the previous unit cell, n-1. When i is the last atom in the unit cell, we consider its interaction with the first atom in the next unit cell, n+1. The first atom and last atom calculations contain an imaginary part due to the interaction of the previous (n-1) and next (n+1) unit cell.

Substituting Equation 2 into Equation 5 gives:

First atom

$$-m_i \omega^2 A_{0,i} = f e^{-ika'} A_{0,i+1} + f_1 A_{0,i-1} - (f + f_1) A_{0,i} \quad (6)$$

Other atoms

$$-m_i \omega^2 A_{0,i} = f A_{0,i+1} + f_1 A_{0,i-1} - (f + f_1) A_{0,i} \quad (7)$$

Last Atom

$$-m_i \omega^2 A_{0,i} = f A_{0,i+1} + f_1 A_{0,i-1} - (f + f_1) A_{0,i} \quad (8)$$

We use equations 5-8 to calculate the motion of all the atoms. Equations 6-8 can be written in matrix form as:

$$\omega^2 M A = D A, \quad (9)$$

where ω is the frequency, M is a mass matrix where $M_{ij} = m_i$ when $i = j$ and $M_{ij} = 0$ when $i \neq j$, A is a vector with $A_i = A_{0,i}$ and D is a matrix consisting of the force constants. Equation 9 can be rewritten in terms of a Hermitian matrix T as:

$$\omega^2 A' = T A', \quad (10)$$

where

$$T = M^{-\frac{1}{2}} D M^{-\frac{1}{2}}, \quad (11)$$

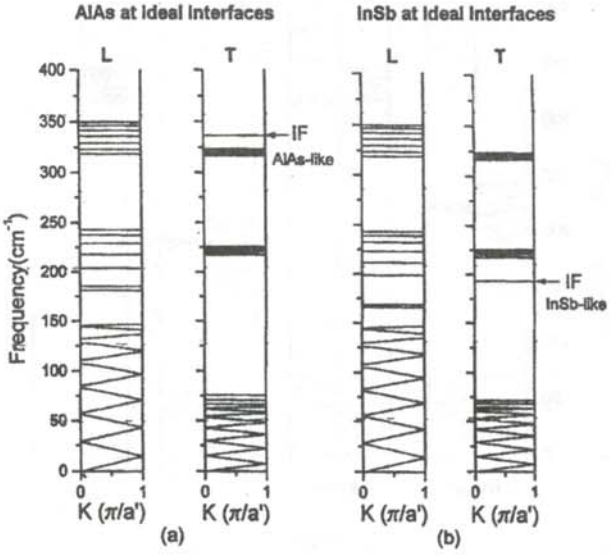

Figure 3

Calculated phonon modes of InAs/AlSb superlattices with two possible ideal interfaces: (a) AlAs-like and (b) InSb-like. The right panels represent transverse modes and the left panels represent longitudinal modes. The interface modes are identified by the letters IF.

and

$$A' = M^{\frac{1}{2}} A. \quad (12)$$

We found the eigenvalues and eigenvectors of the Hermitian matrix, T, using a library subroutine and a FORTRAN 90 program. The eigenvalues, ω^2, of the Hermitian matrix are the squares of the frequencies of the phonon modes. The real and imaginary parts of the eigenvectors are related to the vibration amplitudes by Equation 12.

DISCUSSION

We first calculated the phonon modes for the four bulk materials: InAs and AlSb, the constituent materials of the superlattices and InSb and Al As, two of the possible interface materials. Figure 2 shows the results of our calculations. For each bulk material, we show the longitudinal mode (L) and the transverse mode (T). The frequenices that are below 150 cm^{-1} (in Figure 2 the dotted lines) represent the acoustic modes, the ones above 150 cm^{-1} (in Figure 2 the solid lines) represent the optical modes. When the wavelength is of the mode is much larger than the unit cell and the atoms vibrate in phase with each other it is called an acoustic mode. When the atoms vibrate out of phase with one another, it is called an optic mode.

Because all four of the materials, two bulk materials (InAs and AlSb) and the two interface materials (InSb and AlAs) have similar acoustical frequenicy ranges, the superlattice acoustical frequency range is similar to that of the bulk material. On the other hand, the otical frequency frange for these four materials are quite different. Therefore, the superlattice optical modes will be confined in one of the materials.

Since when we calculate the modes of the bulk material, we took the unit cell to be the same as the superlattices (28 atomic layers), the results are the same as one would get by folding the Brillouin zone for the conventional bulk material fourteen times as the bulk material only has two atoms in the unit cell.

We next studied the superlattices with ideal interfaces and interfaces with switched atomic layers. We followed the techniques used in a previous study of phonon modes in ZnTe/CdSe superlattices. [7,8] The phonon modes calculated for the structure shown in Figure 1(a), (AlAs-like), are shown in Figure 3(a). Figure 3(b) shows the calculated phonon modes for an ideal InSb-like interface. Figure 4 shows the results of the phonon mode calculations for the two possible switches of cation layers about an As layer with two different interfaces: (a) AlAs and (b) InSb.

The possible interface modes are indicated by the label IF in Figures 3 and 4. The interface modes are identified by comparing frequency range of the corresponding bulk material in Figure 2 with the calculated superlattices that have ideal (Figure 3) and switched (Figure 4) interfaces. If the frequency of a superlattice is in the range of either of

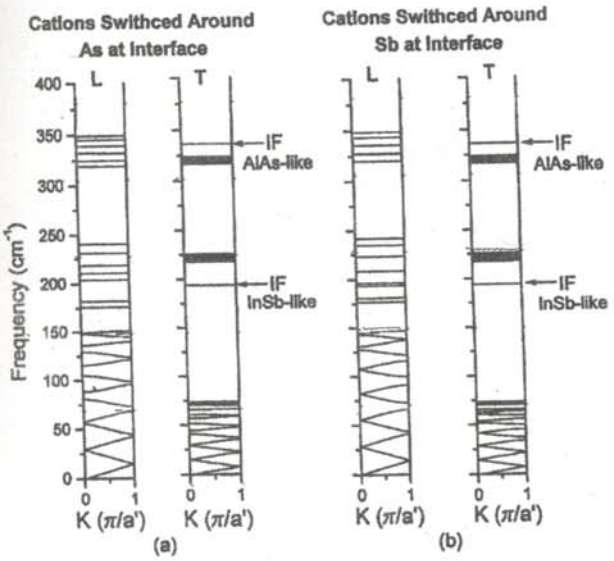

Figure 4

Calculated ;phonon modes of the two possible switches of cation layers around the As layers for superlattices with two different interfaces: (a) AlAs-like and (b) InSb-like. The interface modes are identified for the transverse modes by the letters IF.

the two bulk materials, it is a mode extended to the entire superlattice, and is called an extended mode. If this frequency belongs only to one bulk material, the mode will be confiend to the material and called a confined mode. if the frequency is in the grange of the two of the two interface materials (InSb or AlAs) but not in the range of the bulk material, it is an interface mode. The interface modes of AlAs and InSb are more easily seen in the transverse vibration graphs. Note that there are more interface modes in the superlattices with switched atomic layers than in the superlattices with ideal interfaces.

Figure 5 shows the vibrational amplitudes for particular vibrational frequencies for several different types of phonon modes in InAs/AlSb superlattices. The three displays in Figure 5 are for the superlattice with ideal AlAs interfaces. The top display is for a frequency where the phonon mode is shared by all of the involved material, the vibrational amplitude extends to the entire superlattice. The next display shows a confined mode. The vibrational amplitudes are confined to the InAs layers. The third display shows the transverse interface mode of the superlattice with an ideal AlAs interface. The frequency of this phonon mode is seen in neither InAs or AlSb bulk material. It only belongs to AlAs, so this mode is sharply located at the interface.

When the layers are switched as shown in Figure 1(b), there will be both InSb and AlAs layers at the interfaces. There will also be some thin bulk layers of InAs and AlSb at the interfaces. There will be more interfaces modes in this case, and some bulk modes could also be localized at the interface. Figure 6 shows modes in the superlattice with the switched interface structures shown in Figure 1(b). The first three displays are transverse interface modes, one InSb mode and two AlAs modes where the two AlAs modes have degenerate frequencies and are localized at the two interfaces. The last display shows a confined InAs bulk mode within the thin bulk layers that the switched layers produce at the interface.

We find that the phonon modes for superlattices with ideal sharp interfaces differ from those with switched atomic layers in that the switched superlattices have more interface modes than the ideal interface. This is probably due to the increase in the thickness of the interface due to the switching layers. The phonon modes for the InAs/AlSb superlattice depend on the interface structures.

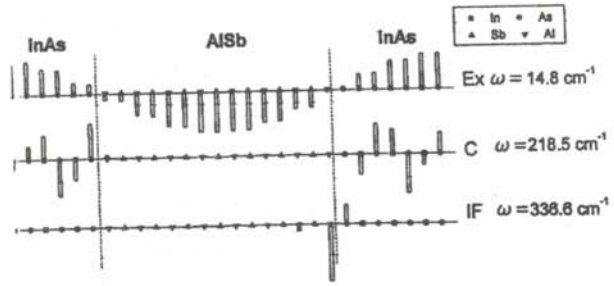

Figure 5

A few different types of modes with both calculated vibrational amplitudes (eigenvectors) and their corresponding vibrational frequencies (eigenvalues) in the InAs/AlSb superlattices. These are for the superlattice with ideal AlAs interfaces where (a) the extended , (b) the confined modes, and (c) the transverse interface modes of the superlattice with AlAs ideal interfaces.

ACKNOWLEDGMENTS

The author would like to thank Brian Mavity for the initial discussion and interest in this study, Haibin Wu for his

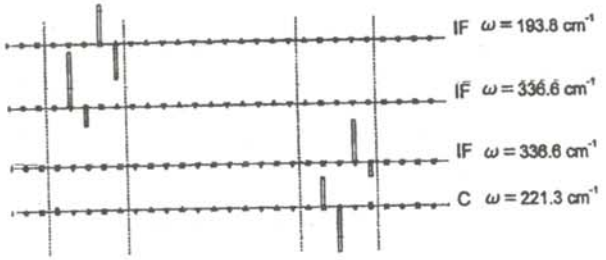

Figure 6

A few different types of modes with both calculated vibrational amplitudes (eigenvectors) and the corresponding vibrational frequencies (eigenvalues) in the InAs/AlSb superlattice. The top three are the transverse interface modes of the superlattice with switched layers of Al and In around As. The bottom display is the confined bulk mode within the bulk layers that are produced by switching layers at the interfaces.

assistance while continuing this research in China and Dr Shang-Fen Ren for suggesting the research topic and advisement. He also would like to thank the Research Corporation and the National Science Foundation for supporting his research.

REFERENCES

* current address of author: 3688 Springlake Circle, Loveland, OH 45140 jmatsko@uiuc.edu.

1. J. Shen, H. Goronkin, J.D. Dow and S. YU. Ren, J. Appl. Phys. 77, (1995), p. 1576.
2. H. Luo, N. Smarth. F.C. Zhang, A. Pareek, M. Dobrowolska, J.K. Furdyna, K. Mahalingam, N. Otsuka, W.C. Chou, A. Petrou and S.B. Qadr, Appl. Phys. Lett., 58, (1991), p. 1783.
3. S.F. Ren and J. Hen, "Ab Initio Pseudopotential Calculations of InAs/AlSb Heterostructures", J. Appl. Phys. 81(3), (1997), p. 1169.
4. A.S. Barker, Jr. J.L. Merz and A.C. Gossard, Phys. Rev. B, 17, (1978), p. 2181.
5. A. Fasolino, E. Molinarfi and J.C. Maan, "Calculated superlattice and interface phonons of InAs/GaSb superlattices", Phys. Rev. B, 33, 12, (1986), p. 8889.
6. Y. Jin, Y.T. Hou, S.L. Zhan, J. Li, S.X. Yuan and G.G.Qin, "Interface vibrational mode in CdSe/ZnTe superlattices", Phys. Rev. B, 45,20, (1992), p. 12141.
7. Z.Z. Xu, H. Dowd, S.F. Ren and Z.Q. Gu, "Phonons in ZnTe/CdSe superlattices with interchange of cation layers across interfaces", J. Phys. Condens. Matt., 9, (1997) p. 1539.
8. S.F. Ren and Z.Z. Xu, "In plane phonons in (001) ZnTe/CdSe stained superlattices", Solid State Communications, 104, 7, (1997) p. 435.

FACULTY SPONSOR

Dr. Shan-Fen Ren
Department of Physics
Campus Box 4560
Illinois State University
Normal, Il 61790-4560
ren@phy.ilstu.edu

SIMPLE CLIMATE MODELING

Suraje Dessai
Department of Environmental Studies
University of Colorado
Boulder, CO 80309
received April 7, 2000

ABSTRACT

Climate models are tools for scientific and policy analysis. Two simple energy balance models (EBM) of the climate of the earth were built for sensitivity studies. Using these models, we demonstrate that: changes in the albedo of the atmospheric-surface system contribute to radiative damping, solar variability is an important contributor to global mean temperature changes; a projection of future global temperatures reveal that by 2100, almost 50% of the greenhouse gas forcing will be due to non-CO_2 greenhouse gases; the projection of global mean temperature changes shows an estimated increase by 2100 between 1 and 2 C; if the greenhouse gases are reduced by 5% (Kyoto Protocol agreement that levels at 2010 be reduced to 1990 levels), we estimate the mean temperature to decrease by 0.5 C by 2100. Evaluation of the one-dimensional EBM show that the simulated values are not significantly different from observed values at the 99% confidence value.

INTRODUCTION

The enhancement of anthropogenic emissions of greenhouse gases (GHG) into the atmosphere is leading to human induced climate changes that are likely to have important impacts on natural and human systems. As a response to this emerging threat, the Kyoto Protocol[1] was signed in 1997, committing developed countries to a 5% reduction of the emissions of a 'basket' of 6 GHGs (to 1990 levels) by the commitment period 2008-2012. To predict the behavior of the climate on variables such as GHGs, climate models are developed. Despite being a young discipline, not yet 30 years old, climate modelers have a great responsibility thrust upon them by the ratification of the United Nations Framework Convention on Climate Change. [2] The objective of this convention is to achieve stabilization of greenhouse gas concentrations in the atmosphere at a level that would prevent dangerous anthropogenic interference with the climate system. [3]

Suraje Dessai is a junior environmental sciences major at the University of Colorado. This research was initiated during his freshman year at the University of East Anglia, Norwich, UK. It won prizes both at the national (in Portugal) and European level under the Young Europeans Environmental Research contests. Suraje is currently working on the first ever climate impact and adaptation assessment for the Portuguese territory. In his spare time, he snowboards in the Rocky Mountains and the Alps.

Our ability to project and detect future climate change is limited by uncertainties regarding:

- estimation of future emissions and biogeochemical cycling (including sources and sinks) of greenhouse gases, aerosols, aerosol precursors, projections of future concentrations of the gases and aerosols, and radiative properties of the gases and aerosols;
- representation of climate processes in models, especially feedback associated with clouds, oceans, sea-ice and vegetation;
- systematic collection of long-term instrumental observations of climate system variables (such as solar output, atmospheric energy balance components, hydrological cycles, ocean characteristics and ecosystem changes) for the purpose of model testing, assessment of temporal and regional variability, and for the detection and attribution studies.

To quantify the response of the climate to changes in forcing, it is essential to account for all complex interactions and feedbacks among the various climate system components. It is not possible to do this reliably using empirical or statistical models, due to the complexity of the system and because the possible outcomes may go well beyond any conditions ever experienced previously. Instead, the response must be found using numerical models of the climate system based upon sound well-established physical principles.

This paper focuses on the study of two energy balance

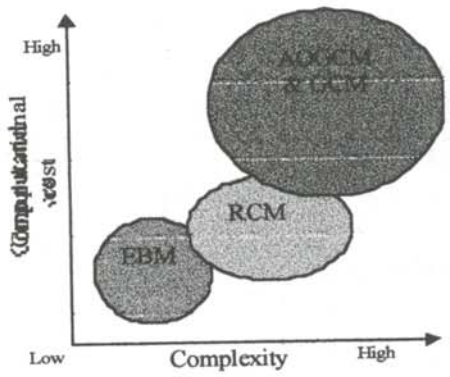

Figure 1
Schematic comparison [4] between different climate models in terms of computational costs and complexity.

models (EBMs), their creation, results from the models and interpretations of the results. The EBMs allow us to predict surface temperature variations with latitude using simplified relationships based on sound physical principles. These models have been instrumental in increasing our understanding of the climate system and in the development of new parameterization methods for evaluating sensitivity for more complex and realistic models. In climate modeling, parameterization is defined as the method of incorporating a process by representation as a simplified function of some other fully resolved variables without explicitly considering the details of the process. [2]

Figure 1 compares various climate models in terms of computational cost and complexity. Computation cost is determined by the computing facilities needed to run the model: personal computer (low) or supercomputer (high). Complexity is the level of detail with which the individual model components are treated. We chose EBMs due to their low complexity and computational costs.

There are more complex and computationally demanding models: circulation models (GCM) and coupled atmospheric-radiative convective models (RCMs), general ocean general circulation models (AOGCM). These complex models can simulate past and present geographical variation of temperature as well as other climatic variables such as rainfall, evaporation, soil moisture, cloudiness and winds. [4] These models provide credible continental scale changes of some of the variables. The use of these models is limited by their high computational costs.

THE MODELS

JavaScript was used to create the models we used. They are available on-line. (http://www.uea.ac.uk/~x9723668/scm/models/model0.html) The first model is a zero-dimensional energy balance model that considers the earth as a single point in space, having a global mean surface temperature of T_s. Viewing the earth from the outside, one observes an amount of radiation input which is balanced in the long term by an amount of radiation output by the planet (i.e., the system is in equilibrium). Since over 70% of the energy which drives the climate system is first absorbed at the surface, the surface albedo will be dominant in controlling the energy input into the climate system. [2]

If α is the average planetary albedo (the reflected fraction of incident radiation), the power absorbed by the earth will be:

$$E_{in} = (1-\alpha)\, S\, \pi R^2, \qquad (1)$$

where S is the solar constant (here considered to be 1370 Wm^{-2}) and R is the radius of the earth. If the earth is assumed to be a blackbody, the power emitted by the earth is given by the Stefan Boltzmann law:

$$E_{out} = 4\pi R^2\, \sigma\, T^4, \qquad (2)$$

where T is the temperature of the earth and σ is the Stefan-Boltzmann constant (5.67×10^{-8} $Wm^{-2}K^{-4}$). For the earth to be in equilibrium, the incoming power (Equation 1) must equal the outgoing terrestrial power (Equation 2). Setting Equation 1 equal to Equation 2 gives:

$$(1-\alpha)\, S\, \pi R^2 = 4\pi R^2\, \sigma\, T^4. \qquad (3)$$

Solving Equation 3 for the radiation balance temperature T, and adding an increment ΔT to model the GHC contribution to the surface temperature, the surface temperature of the earth T_s can be written as:

$$T_s = \sqrt[4]{\frac{(1-\alpha)S}{4\sigma}} + \Delta T. \qquad (4)$$

In our modeling, we assume a value of 33 K for ΔT. Using the model outlined in Equation 4, it is possible to observe the effect of the albedo on the surface temperature of the earth.

A second more complex one dimensional EBM considers each latitude zone of the earth independently. Dividing the earth into latitudes provides a more realistic approach than

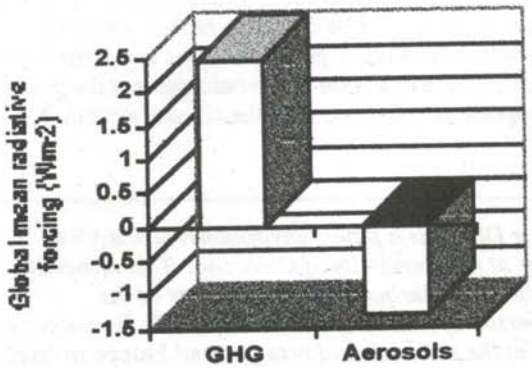

Figure 2
Estimates of the globally and annually averaged anthropogenic radiative forcing due to changed in concentrations of greenhouse gases and aerosols from pre-industrial times to the present . [8]

the first model which only supplies the global mean surface temperature. This model can be accessed at http://www.uea.ac.uk/~x9723668/scm/models/model1.html. The model is controlled by three main relationships:
the radiation entering the earth at latitude ϕ is given by:

$$R_{in}(\phi) = \frac{S}{4} SunWt(\phi), \quad (5)$$

where $SunWt(\phi)$ is the solar radiation distribution at each latitude;
the surface temperature at latitudes ϕ is given by

$$T_s(\phi) = \frac{R_{in}(\phi)[1 - \alpha(\phi)] + (K)(GMT) - A}{B + K}, \quad (6)$$

where $\alpha(\phi)$ is the initial albedo at latitude ϕ, GMT is the global mean temperature (assumed to be 14.87 C) and K,A and B are empirical constants.

The outgoing radiation at latitude ϕ is given by:

$$R_{out}(\phi) = A + (B)T_s(\phi) + (\alpha)R_{in}(\phi). \quad (7)$$

The first part of Equation 7 is the long-wave radiation from the sky to space and the second part is the reflected incoming solar radiation. The albedo of the earth below 70° latitude is assumed to be 0.3, and the ice above 70° latitude will increase the albedo to 0.6.

Definition of terms used in climate modeling
An important aspect of models is 'radiative forcing'. Radiative forcing is the perturbation of the energy balance of the surface-troposphere system after allowing the stratosphere to readjust to a state of global mean radiative equilibrium. [4,5] An example of radiative forcing is the perturbation of the energy balance following a change in the concentration of carbon dioxide or a change in the output of the sun. A positive radiative forcing tends to warm the surface, while a negative forcing tends to cool it. Some external forcings are positive forcing by greenhouse

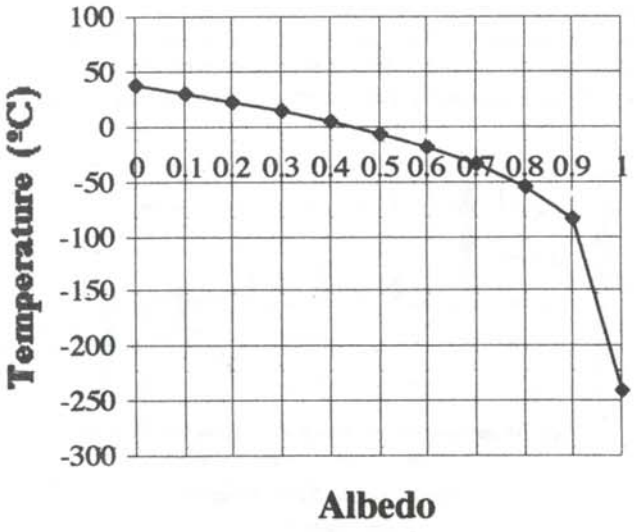

Figure 3
Global mean surface temperature change vs albedo using a zero-dimensional energy balance model.

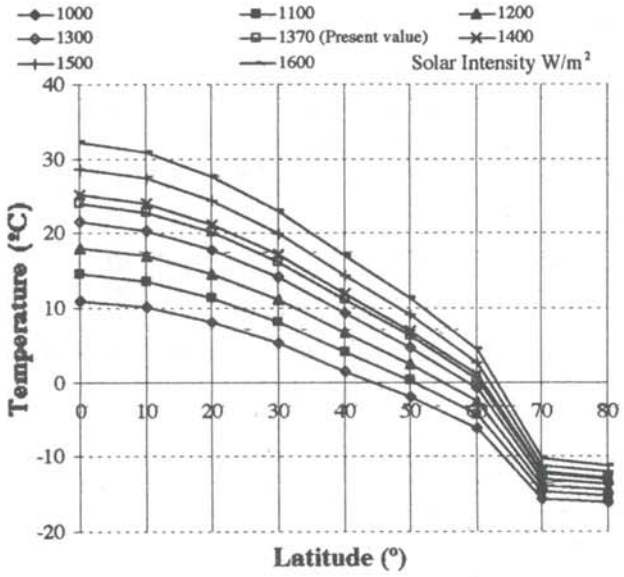

Figure 4
Surface temperature at different latitudes for different solar energy using a one dimensional energy balance model.

gasses (CO_2, CH_4, N_2O, CFC-11, CFC-12 HCFC22 and other halocarbons) at a rate of 2.45 Wm^{-2} and an estimated (within a factor of 2) of negative forcing by aerosols of -1.3 Wm^{-2}. Figure 2 shows the global mean radiative forcing due to two mechanisms, GHG and aerosol forcing, since pre-industrial times. These are the only two mechanisms that have been considered with sufficient confidence to matter in the modeling processes.

'Climate sensitivity' is the steady-state increase in the global annual mean surface air temperature associated with a given global mean radiative forcing. [4] It is common practice to use CO_2 doubling as a benchmark for comparing climate model sensitivities.

The 'feedback term' parameterizes the effects the processes involving water vapor, clouds, ice and snow, and ocean-atmosphere dynamics. [6] In equilibrium,

$$\Delta Q = \lambda \Delta T, \quad (8)$$

where ΔQ represents the external forcing, ΔT is the change in global mean temperature and λ is the atmospheric feedback parameter. An example is the case where the solar absorption does not change. Then the derivative of Equation 1 can be used to find DQ:

$$\Delta Q = \frac{\partial Q}{\partial T} \Delta T = 4\sigma T^3 \Delta T \quad (9)$$

Using Equation 8 and picking an effective emission temperature of 255K gives a value of the feedback term as:

$$\lambda = 4\sigma T^3 = 3.8 \text{ Wm}^{-2}. \quad (10)$$

This value coincides with the one that can be extrapolated by knowing that the minimum global temperature has increased between 0.3 C and 0.6 C since the 19th century [4] and using the radiative forcing shown in Figure 2. Solving

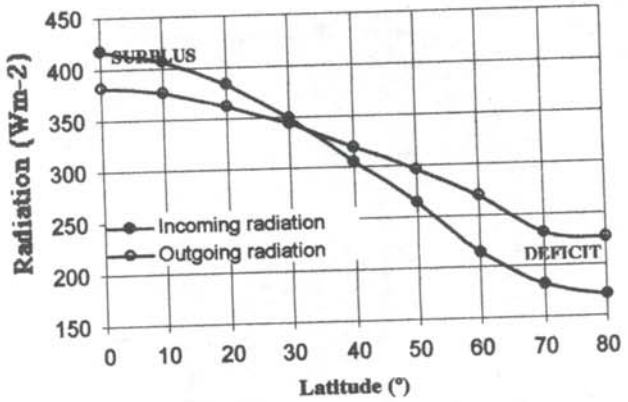

Figure 5

Radiation as a function of latitude using a one dimensional energy balance model.

Equation 8 for λ gives:

$$\lambda = \frac{2.45 - 1.30}{0.3}\ \mathrm{Wm^{-2}} = 3.8\ \mathrm{Wm^{-2}}. \qquad (11)$$

For our modeling, we pick feedback terms of values 1, 2, 3.3 and 3.8 Wm^{-2} and radiative forcing values shown in Table 1. To compare the various climatological perturbations, we found an average value and then found the temperature change the perturbations had forced.

RESULTS

Results from the zero-dimensional EBM are shown in Figure 3. The line shows the temperature vs albedo. As expected, an increase in albedo leads to a decrease in the surface temperature. The earth's actual mean albedo has a value of 0.3, which produces a global mean surface temperature of about 14 C.

The one-dimensional EBM calculated values of surface temperature, incoming and outgoing radiation in each latitude zone. Figure 4 shows the surface temperature at different latitudes with increasing solar energy. A solar energy increase leads to a temperature increase, while a solar energy decrease provokes a temperature reduction. High temperatures can be seen near the equator, while low temperatures are found near the poles. The sudden

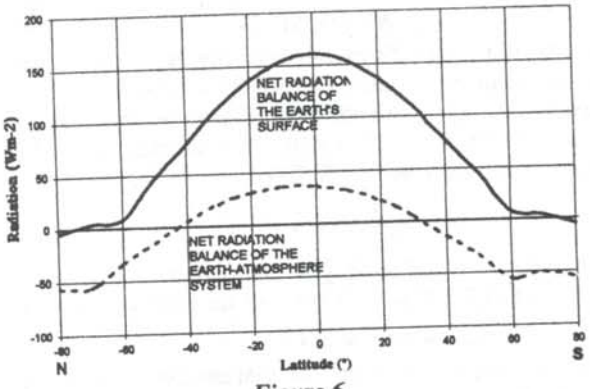

Figure 6

Net radiance balance for the surface of the earth and the whole earth-atmosphere system.

	1980	1990	1994	2100
CO_2	1.10	1.50	1.56	2.83
CO_2+GHG	*1.83*	*2.45*	*2.85*	*5.55*
GHG+aerosols	0.53	1.15	1.55	4.94
Kyoto	0.53	1.15	1.55	3.57

Table 1

Comparison of estimated radiative forcing in Wm^{-2} due to different scenarios which consider: CO_2, all GHGs, all GHGs and aerosols and the Kyoto Protocol agreement with reduction in GHGs emissions

decrease in temperature at a latitude of 70° is due to the change in albedo at this latitude. Figure 5 shows the incoming and outgoing radiation. There is a positive budget (surplus) at latitudes less than 35° and a deficit at larger latitudes. Figure 6 shows the net radiation balance of the earth's surface (incoming solar radiation minus long-wave radiation from sky to space) and the earth-atmosphere system (incoming solar radiation minus outgoing long-wave radiation) as a function of latitude.

Results of how different forcing and feedback factors effect the temperature is shown in Table 2. Figure 7 shows a comparison of the various perturbations using a mean value of $\lambda = 2.65\ Wm^{-2}$, which leads to a climate sensitivity $\Delta T = 1.5$ C (if you only consider doubling CO_2) and $\Delta T = 2.2$ C if you consider all perturbations except clouds (due to its high uncertainty). These results have caveats because: 1) we assume that the climate system is in equilibrium; 2) we assume that the heat flux into the ocean is zero. Both of these assumptions are not true, but they simplify the modeling exercise which otherwise would not a simple task. Taking this into account, we use the best estimate [16] of $\Delta T = 2.5$ C with $\lambda = 1.484\ Wm^{-2}$ and $\Delta Q = 3.71\ Wm^{-2}$. Using these values, we estimate global mean temperature change for the next century (see Figure 8) under various for various forcing combinations: CO_2; CO_2 + GHG; and GHG+aerosols and Kyoto. Notice that the CO_2 and GHG+aerosol forcing curves are in agreement

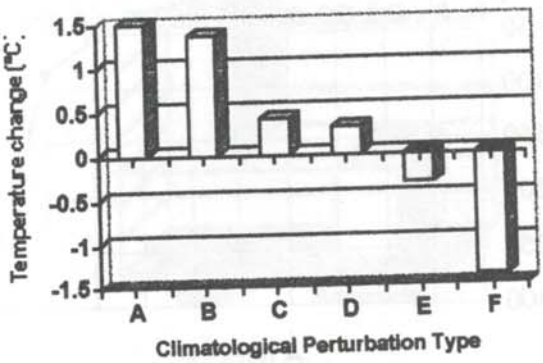

Figure 7

The effect of various climatological perturbations upon surface temperatures using a value of $\lambda = 2.65\ Wm^{-2}$. The perturbations legend is shown in Table 2

		λ ($Wm^{-2}K^{-1}$)			
		3.8	3.3	2.0	1.0
	ΔQ(Wm^{-2})	ΔT (C)			
A-Doubling of CO_2	3.5 : 4.0	0.9 : 1.0	1.1 : 1.2	1.8 : 2.0	3.5:4.0
B-Solar Luminosity (+1%)	3.42	0.9	1.0	1.7	3.4
C- Doubling N_2O	0.97	0.3	0.3	0.5	1.0
D-Tripling CH_4	0.70	0.2	0.2	0.4	0.7
E-Aerosols in Clouds	0.0 : -1.5	0 : -0.4	0 : -0.5	0 : -0.8	0 : -1.5
F-Volcanic Eruptions	-2 : -4	-0.5 : -1	-0.6 : -1.2	-1.0: -2.0	-2 : -4

Table 2
Temperature changes forced by climatological perturbations with different feedback factors.

with the observed global mean temperature change since 1850.

DISCUSSION OF RESULTS

EBM calculations

Figure 4 is in agreement with the fact that the average temperature in not uniform throughout the latitude zones. From Figure 4, one can deduce the changes that might have happened millions of years ago on the earth if variations in the tilt, eccentricity and precession of the earth's orbit lead to changes in the amount of solar energy striking the earth. [11] Incorporation of solar variability improves the agreement between the model and global mean temperature observations. [12]

In the radiation budget calculation shown in Figures 6 and 7, an imbalance between the equator regions and the pole

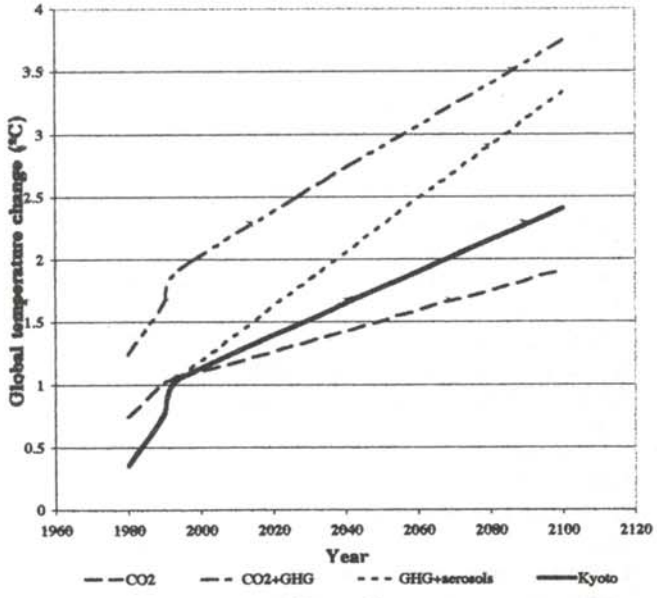

Figure 8
Global mean temperature change for different scenarios for the best estimate of climate sensitivity [11] (2.5 C) from 1980 to 2100.

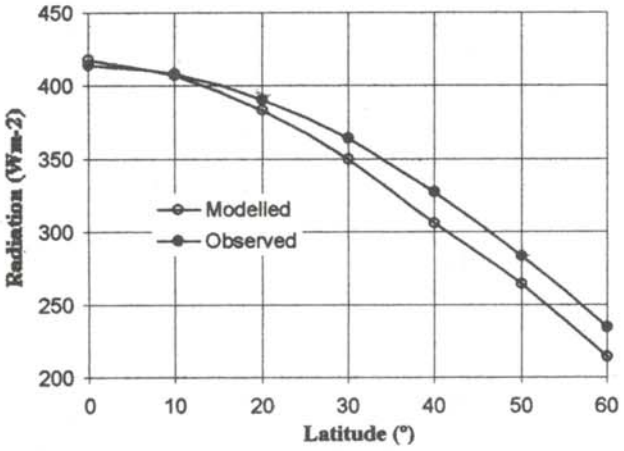

Figure 9
Observed mean short-wave radiation vs latitude [16] compared with simulated values from one dimensional energy balance model.

regions is evident. As the tropics do not get progressively hotter or the higher latitudes colder, a redistribution of world energy must occur, probably taking the form of a continuous movement of energy from the tropics to the poles. [13] The poleward heat transport must take place within the atmosphere and the oceans.

The reliability of the one-dimensional EBM can be seen in Figure 9, by comparing simulated and actual values. The statistical evaluation of the data shows that the simulated values are not significantly different from the observed at the 99% confidence level. The mismatch above 20° latitude is believed to be due to the energy transported from the equator polewards by the general atmospheric circulation and the oceans which is not represented by the model. Figure 10 shows the comparison of the simulated and observed long-wave radiation from the sky to space.

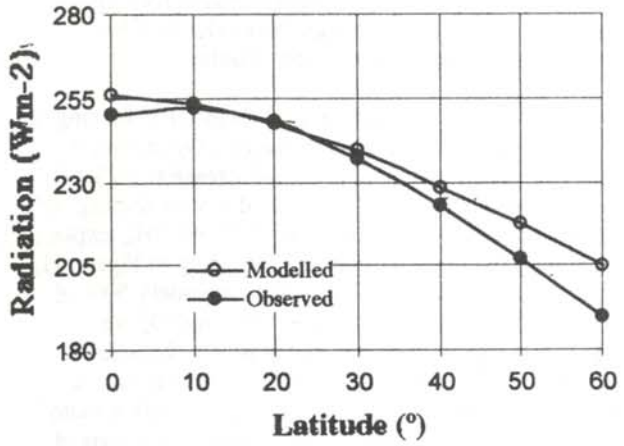

Figure 10
Observed annual mean long-wave radiation from the sky to space for various latitudes [16] compared with the simulated values from a one-dimensional energy balance model.

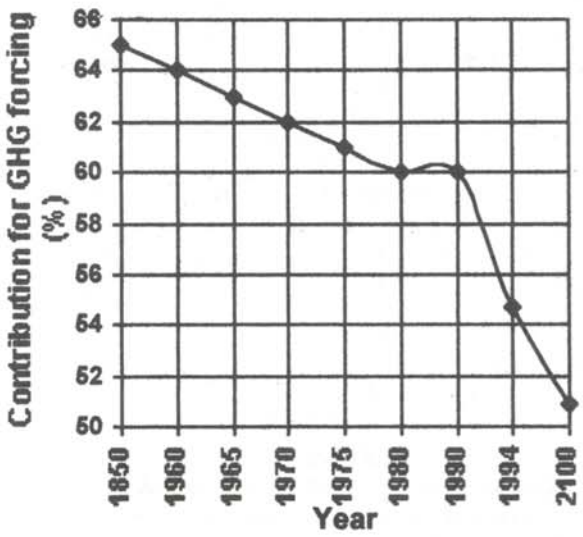

Figure 11
CO_2 contribution to greenhouse has forcing from 1980 to present and projected values to 2100

Again, there is no significant different observed at the 99% confidence level. Modeled values are slightly higher than observed, possibly due to the misrepresentation of the greenhouse effect of clouds by the empirically determined constants used in the equations driving the model.

Radiative Forcing
The global mean temperature change due to different radiative forcing mechanisms have a big range of values due to the uncertainty of the feedback term as well at the size of the forcing.

Figure 7 demonstrates that the combination of GHG forcing over rides other negative forcing because the GHG's have a longer lifetime than aerosols (e.g. N_2O has a life time of about 120 years and a radiative forcing 200 times that of CO_2). Even though the model is rather 'crude', it appears to be moderately reliable.

Calculations of the contribution of CO_2 in GHG forcing is shown in Figure 11. The importance of CO_2 forcing is gradually decreasing, with a sudden decrease from 1960 onwards. Again, the large lifetime and size of forcing, and increase in non-CO_2 GHG, such as N_2O and CH_4, explain this decrease in CO_2 importance. According to Figure 11, by 2100, CO_2 will represent only approximately 50% of the GHG forcing. This means that the non-CO_2 are becoming increasingly important for future climatic changes. The Kyoto Protocol only intends to reduce a 'basket' of six GHG's. Stabilizing CH_4 and N_20 at today's levels produce reductions in anthropogenic emissions of 8% in CH_4 and 50% in N_20 according to our projections. This makes the 5% reduction agreed to in Japan seem to be an irrelevant conquest.

SUMMARY

Although its reliability is still questionable, climate modeling is one of the best tools we have to predict future environmental change. This tool should continue to be investigated to develop mitigation policies designed to minimize the impacts of climate change on human society. The biggest problem in the models is the lack of knowledge about certain climatic processes.

The models created is this project are simple and revealed moderate specificity. We showed that non-CO_2 GHG's are becoming increasingly important in determining future climate changes. Our projection is that the global temperature should increase by around 3 C by 2100. According to projections from our models, the recently agreed upon Kyoto Protocol will diminish this warming by only 0.9 C. These results should be considered with caution since this exercise is oversimplified due to time constraints. We intend to perform a more elaborate exercise in the future.

ACKNOWLEDGMENTS

The author would like to thank Fundação da Juventude and young European's Environmental Research organizers for the incentive and funding to do this project. He is indebted to Dr. Sarah Raper for comments on this paper and to Dilan Jayasuriya for helping proofread it. Finally, he wishes to thank Routledge for partially sponsoring the research that made this paper possible.

REFERENCES

1. Kyoto Protocol to the United Nations Framework Convention on Climate Change, Conference of the Parties, 3rd Session, U.N. Doc. FCCC/CP/1997/L.7/ Add.1 (1997), reprinted in 37 I.L.M. 22 (1998).
2. McGuffie, K. and A. Henderson-Sellers, A Climate Modeling Primer, John Wiley & Sons (1997).
3. United Nations Framework Convention on Climate Change (1992). *Article 2.*
4. Harvey, D., J. Gregory, M. Hoffert, A. Jain, M. Lal, R. Leemans, S. Raper, T. Wigley and J. de Wolde, "An Introduction to Simple Climate Models used in the IPCC Second Assessment Report". In Houghton, J.T., L.G. Meira Filho, D.J. Griggs and K. Maskell (eds.) IPCC Technical Paper II, Intergovernmental Panel on Climate Change (1997).
5. Houghton, J.T., L.G. Meira Filho, B.A. Callander, N. Harris, A. Kattenberg and K. Maskell, Climate Change 1995: The Science of Climate Change. Contribution of Working Group I to the Second Assessment Report of the Intergovernmental Panel on Climate Change, Cambridge University Press (1996).
6. Ramanathan, V., Ambio, 27, (1998), pp. 187-197.
7. Schimel, D., D. Alves, I. Enting, M. Heimann, F.Joos, D. Raynaud, T. Wigley, et al., "Radiative Forcing of Climate Change", in Houghton, J.T. *et al.* (eds). Climate Change 1995: The Science of Climate Change, Cambridge University Press, (1996), pp. 65-132.
8. Kattenberg, A., F. Giorgi, H. Grassl, G.A. Meehl, J.F.B. Mitchell, R.J. Stouffer, T. Tokioka, A.J. Weaver and T.M.L. Wigley, "Climate Models – Projections of Future Climate", in Houghton, J.T. *et al.* (eds). Climate

Change 1995: The Science of Climate Change, Cambridge University Press, (1996), pp. 285-357.
9. Schimel, D., M. Grubb, F. Joos, R. Kaufmann, R. Moss, W. Ogana, R. Richels and T. Wigley, "Stabilization of Atmospheric Greenhouse Gases: Physical, Biological and Socio-economic Implications", in Houghton, J.T., L.G. Meira Filho, D.J. Griggs and K. Maskell (eds.) IPCC Technical Paper III, Intergovernmental Panel on Climate Change (1997).
10. Wigley, T.M.L., A.K. Jain, F. Joos, B.S. Nyenzi, P.R. Shukla, "Implications of Proposed CO_2 Emissions Limitations", in Houghton, J.T., L.G. Meira Filho, D.J. Griggs, K. Maskell (eds.) IPCC Technical Paper, Intergovernmental Panel on Climate Change (1997).
11. Dawson, A.G., Ice Age Earth: late Quaternary Geology and Climate, Routledge, (1992), pp. 235-256.
12. Gordon, A., W. Grace, P. Schwerdtfeger and R. Byron-Scott, Dynamic Meteorology: a Basic Course, Arnold (1998), pp. 256-313.
13. Barry, R.G. and R.J. Chorley (7th ed.), Atmosphere, weather and climate, Routledge, (1998).
14. Gates, W.L., A. Henderson-Sellers, G.J. Boer, C.K. Folland, A. Kitoh, B.J. McAveney, F. Semazzi, N. Smith, A.J. Weaver and Q.C. Zeng, "Climate Models – Evaluation", in Houghton, J.T. *et al.* (eds). Climate Change 1995: The Science of Climate Change, Cambridge University Press, 229-284
15. Wigley, T.M.L., S.C.B. Raper, "Future Changes in Global Mean Temperature and Sea Level", in Warrick, R.A., E.M. Barrow and T.M.L. Wigley (eds.) Climate and Sea Level Change: Observations, Projections and Implications, Cambridge University Press, (1993), pp. 111-133.
16. Linacre, E. and B. Geerts, Climates and Weather Explained, (Routledge),1997; Myhre, G, Highwood, E.J., Shine, K.P., and Stordal, F. "New Estimates of Radiative Forcing Due to Well Mixed Greenhouse Gasses", Geophys. Res. Lett., 25, pp. 2715-2718.

FACULTY SPONSOR

Dr. Sarah Raper
Climatic Research Unit
University of East Anglia
Norwich NR4 7TJ England
S.Raper@uea.ac.uk

BODY VIBRATIONAL SPECTRA OF METAL FLUTE MODELS

Clare M. Hurtgen *
Physics Department
Duke University
Durham, NC 27708
received March 25, 2000

ABSTRACT

For years, flutist have argued over the tonal advantages of using different precious metals for their instruments. Occasionally, scientists have entered the fray and attempted to offer an objective point of view based on experimental measurements, However, their research often involved actual instruments and performers, ignoring variations in wall thickness, craftsmanship and human consistency. These experiments were conducted using a variety of methods; all concluded that the wall material has no effect on the tone. This paper approaches the question using simple tubular models, excited by a wind source through a fipple mouthpiece. The amplitude and phase of the harmonic components of the body vibrational signal are measured with a stereo cartridge. The results show a complex pattern of wall vibrations in the vicinity of a tone lattice at frequencies that match significant harmonics of the air column. The tube wall was found to expand in a nonuniform or 'elliptical' manner due to the asymmetry of the tone holes.

INTRODUCTION

Modern flutes are made from a variety of metals and alloys, including nickel silver, sterling silver, 5-14K gold, platinum and titanium. The choice of wall material is often the subject of a fierce debate between professionals with different personal preferences. Instrument manufacturers have an obvious monetary stake in maintaining the market for the more expensive materials. Flutists most often describe the timbre of the silver flute as 'brighter' than that of the 'darker' gold flute. These aural impressions are based on the perceived harmonic content. It is accepted (one might argue assumed) within the community of professional flutists that the wall material has a significant, if not dominant, effect on the timbre of the tone produced. However, there is no scientific documentation of this phenomenon. In fact, scientists who have investigated the question have all reached the same conclusions: that the wall vibrations are negligible and the wall material has no effect on the flute tone.

Clare graduated magna cum laude from Duke University in May 1999, with a double major in physics and music. This research was conducted during her senior year as an independent study laboratory course, qualifying as a senior thesis for Graduation with Distinction in Physics. The results were presented in 1999 at the conferences of the American Physical Society in Atlanta and the North Carolina Regional Chapter of the Acoustical Society of America in Raleigh. As an undergraduate, Clare was the principal flutist of the Duke Univesity Wind Symphony and Symphony Orchestra, and a student of Brooks de Wetter-Smith of the University of North Carolina-Chapel Hill. Clare is currently employed as an architectural acoustics consultant at Jaffee Holden Scarbrough Acoustics, Inc. in Norwalk, CT.

The earliest research that addressed the body vibrations of woodwind instruments was published in 1964. [1] The clarinet was the initial subject of this investigation, but the work was extended to other members of the woodwind instrument family. In the case of the flute, it was noted that the magnitude of the body vibrations was smaller than that of the reed instruments. Four flutes were used in this experiment : 0.012" coin silver; 0.014" gold; 0.020" coin silver ; and a silver alto flute. The magnitude of the body vibrations was measured at several locations and for several pitches at 3 in. from the embouchure hole. After comparing the values to the sound level at a distance of 1 foot from the instrument, it was determined that any radiated sound from the body vibrations was inconsequential when compared to the amplitude of the normal sound produced.

The seminal research in the field was published in 1971. [2] Three keyless flutes of 0.036 cm silver, 0.153 cm copper and 0.41 cm grenadilla wood were constructed. Identical plastic headjoints were attached to each flute. In a listening trial, a musical phrase was played three times behind a screen and the participants in the study were asked to identify which repetition was performed on a different instrument. For a performing trial, the three flutes were attached to a rotating apparatus in such a

manner that the player could see only the identical headjoints and could not identify which instrument was currently in use. The participants played the three unseen flutes and indicated their personal preference. The apparatus was spun and the participants were asked to identify their original selection. Subsequent statistical analysis concluded that the success rate for both trials differed only slightly from the expected results for random guessing.

The effects of wall material were studied in a doctoral thesis in 1980. [3,4] Five flutes were constructed by the same manufacturer to have identical lengths, bore diameters, wall thickness, embouchure holes and tone holes. Wall material (palladium, white gold, 14K gold and two of sterling silver) and its subsequent weight were the only remaining variables across the set of flutes. Two professional flutists played the performance tasks on each of the five flutes inside an anechoic chamber. The performers were asked to play three pitches (G in each of the three registers of the flute) at two dynamic levels. Two condenser microphones in the anechoic chamber were connected to a spectrum analyzer. The harmonic content of the sound differed only between performers.

In 1990, a team in India observed body vibration patterns using conventional holography to produce time-averaged interferograms. [5] The instruments used were Indian flutes made of reed with 8 finger holes. The flutes were excited by an air ribbon through a mouthpiece made of glass and rubber and lightly clamped at both ends. The vibration patterns for different fingering configurations, frequencies and blowing pressures were reported but not interpreted.

In 1998, a study analyzed impulse responses in the time and frequency domains using a microphone positioned inside a flute. [6] Only two instruments were used, a nickel silver/copper alloy Bundy flute and a silver Muramatsu flute. The Bundy flute was found to be more 'reverberant', while the Muramatsu had more high frequency components. No change was observed for different microphone positions. The authors noted the 'remarkable difference between the two flutes in tone quality', but did not comment on its origin or possible consequences.

Numerous demonstrations have been given within the community of professional flutists. On several occasions, Coltman played on a concrete flute behind a screen and the audience was completely unaware. At the National Flute Association convention in 1998, James Galway performed on an array of flutes of different materials, all manufactured by Muramatsu. However, these exhibitions were never intended to be scientifically rigorous and the results were never published.

THE EXPERIMENT

Design Goals

The previous experiments were conducted using a variety of methods, but there are three recurring problems:

- The use of real instruments introduces several additional variabales that are often left uncontrolled. Flutes of different materials have different standard wall thickness. Instruments in different price ranges, as dictated by the choice of material, have varying levels of craftsmanship.
- The use of live performers raises questions about skill level, consistency and possible bias of the player. This makes the results difficult to reproduce. The flutist's embouchure is the arrangement of the lips necessary to produce a sound. It involves varying the shape and tension of numerous muscles in the lips, mouth and jaw. It is extremely difficult, even for a professional player, to reset the embouchure on a different instrument and produce a tone in exactly the same manner.
- The data collected in the experiments were primarily qualitative, in the form of listener identifications or descriptions.

To address these concerns, the following design goals were identified:

1. Eliminate the additional variables present on actual flutes through the use of tubular models.
2. Ensure reproducibility of results with an artificial air supply.
3. Collect quantitative data with an oscilloscope and spectrum analyzer.

Tubular Models

A set of four models was constructed of standard stainless steel tubing (due to its availability and low cost) to examine the effect of tone holes on wall vibration. This thin-walled material was chosen to provide a large output signal. The models closely approximated the characteristic dimensions of an actual instrument as shown in Table 1.

Tube A had no tone holes and was used as a reference or control model. Tube B had 1 tone hole at the position corresponding to the first open tone hole on an actual flute. Tube C had the set of 6 tone holes necessary to play a diatonic scale. Tube D had the set of 9 tone holes necessary to play a chromatic scale. The spacing between tone holes was not exactly even, but increased slightly toward the foot of the model, as on a real flute.
The effective length of each of the tubes was determined by measuring the frequency of the tone produced by each

Dimension	Flute inches	Models inches
Length (excluding headjoint)	20.53	20.53
Bore diameter	0.748	0.750
Tone hole diameter	0.59	0.60
Wall thickness	0.010-0.18	0.010

Table 1

Body dimensions of a standard flute and our tubular models.

of the models. The length was calculated from:

$$L_{eff} = \frac{n\,v}{2\,f} \qquad (1)$$

where $n = 1$ is the harmonic number, $v = 343$ m/s is the speed of sound in air at room temperature and f_1 is the fundamental frequency. Consider Tube A. With a length of 20.53 in (without mouth piece), it should have a fundamental frequency of 329 Hz. The measured value of 540 Hz occurs because we are resonating at the first harmonic (one octave above the fundamental) due to the air pressure. So, Tube A has a fundamental frequency of 540/2 = 270 Hz. From Equation 1, this implies an effective length of 25 in. Thus, the mouthpiece introduces a length correction of 4.5 in.

The effective lengths of Tubes B,C and D are significantly shorter than 20.53 in due to the presence of the tone holes. The first open tone hole on each of the models is located 6 in. from the end of the tube. This distance, in addition to the mouthpiece correction, yields effective lengths of approximately 10.5 inches for Tubes B-D, in agreement with the calculations in Table 2.

It should be noted that the most significant difference between the models and the real flute is the design of the tone holes. The tone holes of the models were simply cut into the metal tubing. On an actual instrument, the keys rest atop a small segment of tube that is drawn or rolled up around the tone holes. This simplification was unavoidable for the purposes of this experiment. While the drilled tone holes do remove some of the variations in craftsmanship, they are also somewhat removed from a realistic situation.

Equipment

A small fan was used as the air supply, regulated by a bellows-type apparatus as shown in Figure 1. An inner box of cardboard was allowed to move freely inside an outer box of plywood, acting as a pressure regulator. The air output was piped directly into the mouthpiece of the model.

A fipple mouthpiece, rather than a flute headjoint, was chosen to stimulate sound production in the models (see Figure 2). Fipples are normally found on whistles, recorders and organ pipes. In this case, a fipple was used to avoid the complications and ambiguities involved in modeling an artificial embouchure. The fipple mouthpiece

Model	Frequency Hz	Effective Length inches
Tube A	540.0	12.50
Tube B	637.5	10.59
Tube C	647.5	10.43
Tube D	645.0	10.47

Table 2

Frequency produced by the various tubes and the calculated effective length of the models.

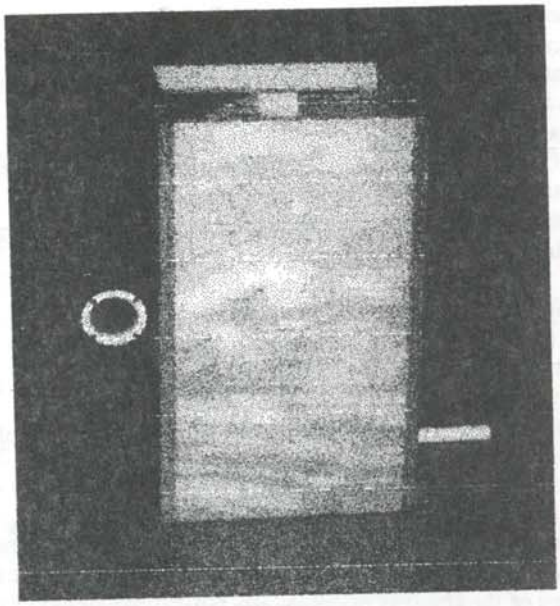

Figure 1

Air supply fan and pressure regulating apparatus.

for this experiment was taken from a standard Yamaha soprano recorder, made of plastic and slightly bored out for a snug fit with the tubular models.

The model was supported at the fipple end of the tube to allow the body to vibrate freely. The tube extended vertically, as shown in Figure 3, eliminating any torque due to gravity. This means of support allowed for easy access from all azimuthal angles.

A stereo cartridge [7], such as that normally found on a record player, was mounted on a lever arm that could rotate freely around a horizontal cross-bar. This arrangement allowed the stereo cartridge to be in light contact with the wall of the tube without damping any possible vibration. The lever arm was adjusted to provide enough pressure to displace the stylus without clipping or distorting the signal.

The signal from the stereo cartridge was passed through a

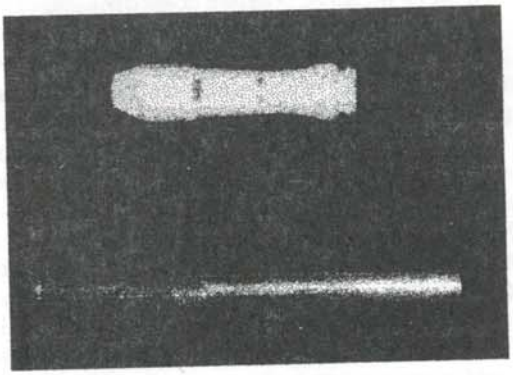

Figure 2

Fipple mouthpiece (top) and a flute headjoint with embouchure hole (bottom).

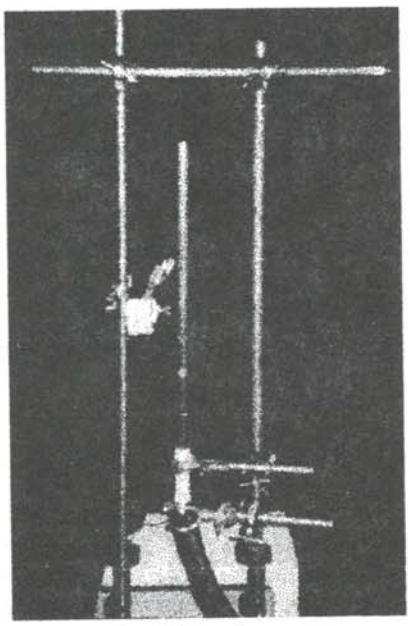

Figure 3

Vertical support system for the model flute. The support at the fipple end allows the body to vibrate freely and gives easy access from all azimuthal angles.

pre-amplifier [8] and displayed simultaneously on an oscilloscope and a spectrum analyzer [9]. The oscilloscope was triggered by the auditory signal picked up by a microphone [10] located at the first open tone hole of the model at an angle of 45°. A cathetometer was used to measure the relative position of the stereo cartridge with respect to a fixed reference point. Figure 4 is a schematic diagram of our system.

We modified the design shown in Figure 4 to investigate the phase relationships of the wall vibrations. Two stereo cartridges were used to measure the relative phase between different points on the walls of the models. The cartridges were calibrated using a mechanical vibrator driven by a function generator. We found that there was no phase shift between the signals of the two cartridges. The signals from each of the cartridges were passed through identical band-pass filters [11] to isolate one harmonic.

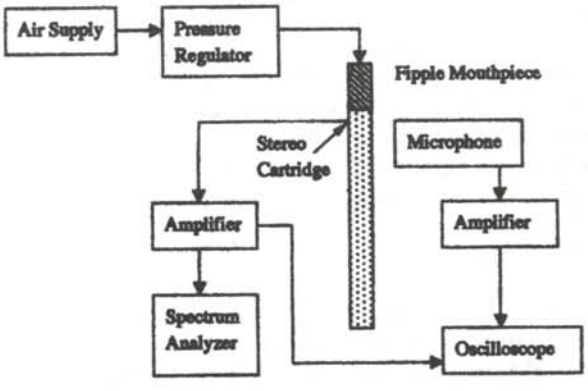

Figure 4

Schematic diagram of the experimental apparatus. A second stereo cartridge was later added to measure relative phases of the wall vibrations.

Although the experiment was conducted in the sub-basement on the building slab, significant interference from external vibration was encountered. The noisy air supply was isolated in a separate room and an intermediate joint on the air supply hose was mechanically grounded to the building slab. The entire apparatus was supported on cement blocks. The vertical ring stands were clamped to these blocks and counter-braced for rigidity. The stereo cartridge lever arm was electrically grounded to the building's water supply. These precautions resulted in clean signals.

DATA

The body vibrations were measured at intervals of approximately 1 in. along the length of each model at two azimuthal orientations relative to the axis of the tone holes (180° or 'the back' and 90° or 'the side'). Typical output signals fed into the oscilloscope had peak-to-peak amplitudes of approximately 40 mV. The amplitudes of the harmonic components of the signal were measured using the spectrum analyzer. We found first, third and fourth harmonics, corresponding to the harmonics of the acoustical signal in air. The data points were normalized and fit to curves.

Figure 5, showing the value of the third harmonic at the two azimuthal orientations at different distances from the fipple end of Tube B, illustrates the reproducibility of the results. The single tone hole is located at the 6 in. position on the tube.

The shape of the curves in Figure 5 can be understood by considering the structure of Tube B. The air pressure fluctuations in the tube have minima imposed by boundary conditions near the open tone hole and the end of the tube. These are coincident with the tube wall displacement maxima evident at these locations. The mechanical coupling to the fipple mouthpiece corresponds to a tube wall displacement minimum at 1 in. on the graph (the

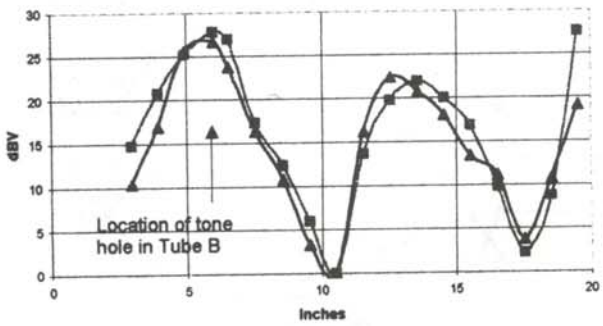

Figure 5

Amplitude of the third harmonic vs distance along Tube B. The location of the first tone hole is marked on the diagram.

effective end of the air column is at about -4.5 in. with respect to the scale on the graph). The other displacement minima are determined by the effective length of 10.6 in. One minima should be at this distance from the end of the tube and the other at this distance from the center of the tone hole.

The two lines on Figure 5 are identical, given the uncertainties of the experimental measurements. This implies that the wall vibrations of the model flute are independent of azimuthal orientation. This is consistent with the relatively small bore perturbation introduced by a single tone hole.

In general, the vibrational spectrum *is* dependent on the orientation in the presence of a tone hole *lattice*. Figure 6 shows the first, third and fourth harmonics measured at the side of Tube C (90° relative to the axis of the tone holes) and the vibrational spectrum for the back (180°). The back spectrum shows a less complex structure than the side spectrum. This indicates greater freedom to vibrate along the side of the tube that is nearest to the tone holes.

It should be noted that the third harmonic of Tube C (shown in Figure 6) displays the same basic structure as that of Tube B (Figure 5). The vibrational minima occur at the fipple mouthpiece (1 in.), around the midpoint of the length of the tube (10 in. - 12 in.) and close to the free end

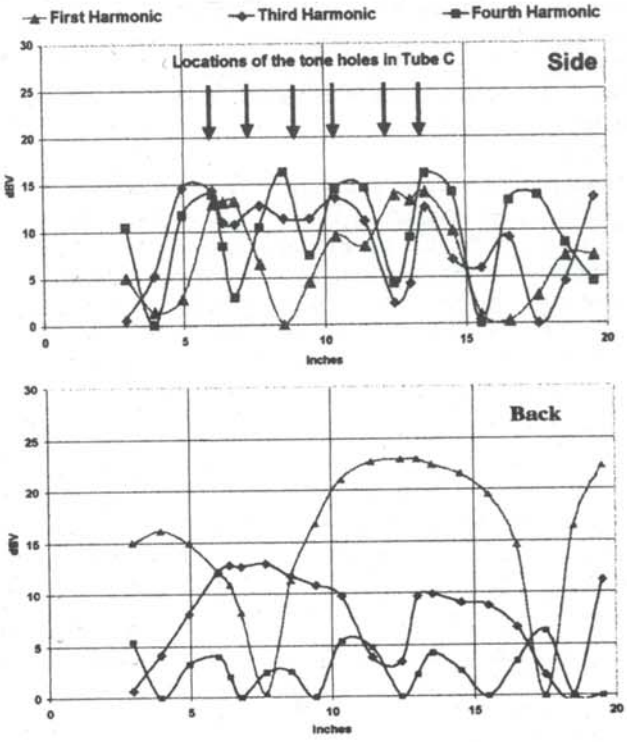

Figure 6
First, third and fourth harmonics as a function of distance along Tube C. The top graph is measured at the side of the tube and the bottom is measured at the back of the tube.

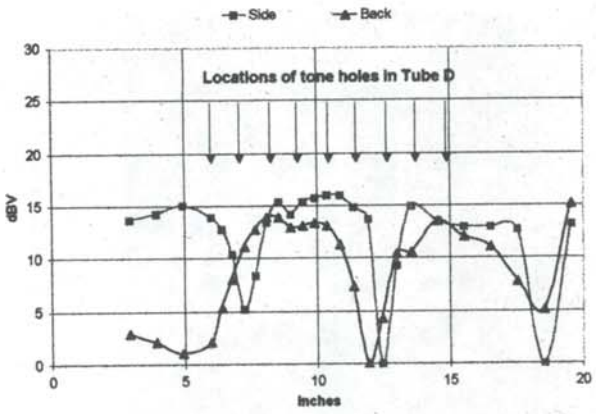

Figure 7
Amplitude of the third harmonic at both orientations on Tube D.

(17 in. - 18 in.) The third harmonic for Tube D (shown in Figure 7) also follows this pattern, although the overall structure is quite different. This may be due to the more regular spacing of the 9 tone holes on Tube D.

These patterns should not be interpreted as elastic modes within the metal itself. The velocity of sound in stainless steel is 0.233 in/μsec [12], so the corresponding wavelength is well over 300 inches. There should be no standing wave modes in the tube walls on the scale of these models.

Phase Relationships

The third harmonic was isolated for this study because this frequency is on the order of the cutoff frequency of the model tube. Above this frequency, the waves (in air) propagate down the entire length of the tube.

One of the stereo cartridges was kept in a fixed position (90° from the tone holes). The other stereo cartridge was moved along the length of each tube on the other side (270°) and at the back (180°). The fixed signal was used as the trigger for the oscilloscope. Using this set up, we could locate each phase reversal between the vibrations on either side of the tube within a region of 0.4 in. An example is shown in Figure 8 which shows the third harmonic amplitude data for Tube B superimposed on the phase data. The scale on the left is the amplitude and the scale on the right is relative phase. When tghe cartridges were located at the same relative position along the length of the tube, the signals were in phase, but the signal at the back was 180° out of phase. The phase reversals were also found to correspond with the pronounced minima of the vibrational signal.

These phase relationships hold true for the more general tone hole lattices of Tubes C and D. This implies that the vibrational harmonics observed were pure modes. It begins to provide a picture of how the tube wall vibrates. For a cylindrical tube, such as the reference model Tube A, one would expect to find uniform circular distortions of the tube's cross section as shown in the top of Figure 9.

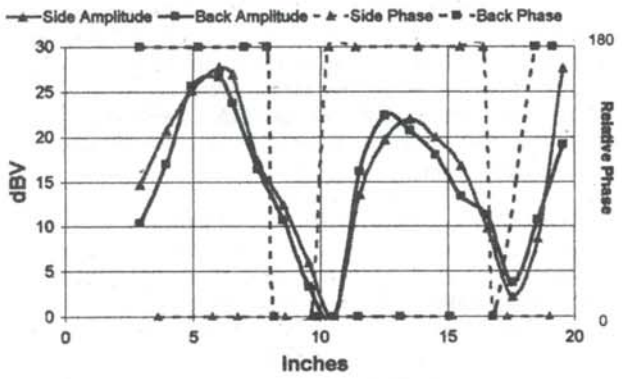

Figure 8
Amplitude vs position and relative phase vs position for the third harmonic on Tube B.

The phase relationships of Tubes B, C and D suggest that the open tone holes introduce a significant azimuthal asymmetry. The cross sections of these tubes undergo non-uniform 'elliptical' distortions as shown in the bottom of Figure 9. The scale and spatial distribution of the phase reversals imply that they could affect upper harmonics differently. This could provide a mechanism for the wall vibrations to affect the tone produced.

ACKNOWLEDGMENTS

Many thanks to Dewey Lawson, without whom this project could not have been started, let alone completed. Also, thanks to Daniel Gauthier and Stephen Teitsworth for advice and technical assistance.

This research was financed by two Undergraduate Research Support grants, administered by Mary Nijhout, Associate Dean for the Natural Sciences. The author was also the recipient of a student travel grant from the American Physical Society. Laboratory space and equipment were provided by Calvin Howell and the Advanced Laboratory course. The band-bass filters were loaned by David W. Smith. The tubular models and the second stereo cartridge assembly were constructed by the Physics Instrument Shop.

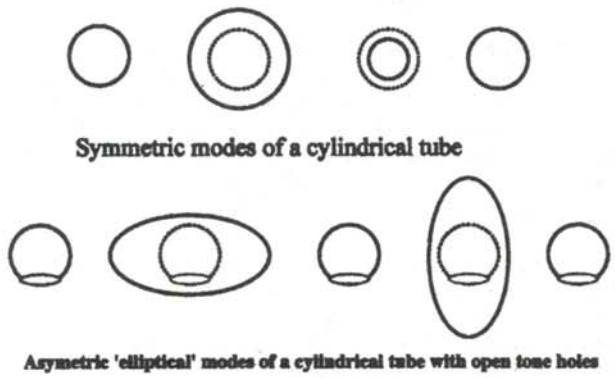

Figure 9
Possible modes of oscillation of the wall of a cylindrical tube. The top is a symmetric mode, the bottom the 'elliptical' mode which we detected.

REFERENCES

* Current Address of Author: 98 Soundview Avenue, A2, Norwalk, CT 06854, churtgen@jhsacoustics.com
1. Backus, John, "Effect of Wall Material on the Steady-state Tone Quality of Woodwind Instruments", J. Acous. Soc. Am., 36, 10, (1964) pp. 1881-1887.
2. Coltman, J.W., "Effect of Material on Flute Tone Quality", J. Acous. Soc. Am., *49*,2, (1971), pp. 520-523.
3. White, J.L., "A Spectral Analysis of Tones Produced on Five Flutes Constructed of Different Metals", Thesis-University of North Carolina Greensboro, University Microfilms (No. 81:144886), Ann Arbor, (1980).
4. White, J.L., "Flute Tone Quality: Does the Metal Make a Difference?", The Instrumentalist, (May 1989), p. 72-73.
5. Kumar, P.T. Ajith,Thomas,P.J., and Purushothaman, C., "Flute Vibrations by Holographic Interferometry", Applied Optics, 29, 19, (1990), pp. 2841-2842.
6. Cocchi, A. and Tronchin, L., "Material and Obsolescence on Flute Quality", http://ciarm.ing.unibo.it, (1998).
7. Stereo Cartridge: Audio Technica Studio Reference Series 1001.
8. The pre-amplifier is a microphone channel on a Realistic stereo mixing console.
9. BK Precision 20 MHz Oscilloscope 1522 and Hewlett Packard 3561A Dynamic signal analyzer.
10. Microphone is Realistic Catalog Number 33-1063.
11. Krohn-Hite model 3202R band pass filter
12. Radiatronics NDT, Inc., "On-line Guides: Sound Velocity Tables: Stainless Steel", http://www.radiatronics.com/guide_vel_stain.htm.

FACULTY SPONSOR

Dr. Dewey Tull Lawson
Senior Scientist and Assistant Director
Center for Auditory Prosthesis Research
Research Triangle Institute
3040 Cornwallis Road
Research Triangle Park, NC 27709-2194

Adjunct Professor of Physics
Duke University
Durham, NC 27708-0305

PREPARING A MANUSCRIPT FOR PUBLICATION

Rexford E. Adelberger, Editor

Perhaps the most important thing for you to keep in mind when you write a manuscript which you intend to submit for publication to the Journal of Undergraduate Research in Physics is that the audience that will be reading the paper is junior or senior physics majors. They are knowledgeable about physics, but unlike you, they have not spent as much time trying to understand the specific work which is being reported in your paper. They also can read English well, and expect the paper to be written by a colleague, not a robot or an 'all-knowing' computer. There is a big difference between the comments you write in the margin of your lab notebook or what you might write in a technical brief and what you should present in a paper for publication in a scientific journal.

There is a significant difference between a Journal article and keeping a journal. Your laboratory data book should be the journal of what you did. It contains all the data, what you did (even if it was an attempt that turned out to be wrong), as well as comments as to what you were thinking at that time. The Journal article is an discussion of how you would do the research without excursions along blind alleys and hours spent collecting data that were not consistent. The reader does not have to be able to completely reproduce the work from the Journal article. The reader should be able to understand the physics and techniques of what was done.

How a person uses Journal articles to find out about new ideas in physics is often done in the following way. A computerized search, using key words in abstracts, is performed to find what work others have done in the area of interest. If the abstract seems to be about the question of interest, the body of the paper is tracked down and read. If the reader then wants to find out the finer details of how to reproduce the experiment or the derivation of some equation, the author of the paper is contacted for a personal in-depth conversation about the more subtle details.

The general style of writing that should be followed when preparing a manuscript for publication in the Journal is different from what you would submit to your English literature professor as a critique of some other work. The narrative of the paper is intended to do three things: 1) present the background necessary for the reader to appreciate and understand the physics being reported in the paper; 2) discuss the details of what you did and the implications of your work; 3) lead the reader through the work in such a way that they must come to the same concluding points that you did. When finished with your paper, the reader should not have to go back and try to decide for themselves what you did. Your narrative should lead them through your work in an unambiguous manner, telling them what to see and understand in what you did. The interpretation of the data or calculations should be done by the writer, not the reader. The interpretation of your results is the most important part of the paper.

You should take care to make sure that the material is presented in a concise logical way. You should make sure that your sentences do not have too many dependent clauses. Overly complicated sentences make the logic of an argument difficult to follow. You should choose a paragraph structure that focuses the attention of the reader on the development of the ideas.

A format which often achieves these aims is suggested below:

ABSTRACT : An abstract is a self contained paragraph that concisely explains what you did and presents any interesting results you found. The abstract is often published separately from the body of the paper, so you cannot assume that the reader of the abstract also has a copy of the rest of the paper. You cannot refer to figures or data that are presented in the body of the paper. Abstracts are used in computerized literature searches, so all key words that describe the paper should be included in the abstract.

INTRODUCTION: This is the section that sets the background for the important part of the paper. It is not just an abbreviated review of what you are going to discuss in detail later. This section of the narrative should present the necessary theoretical and experimental background such that a knowledgeable colleague, who might not be expert in the field, will be able to understand the data presentation and discussion. If you are going to use a particular theoretical model to extract some formation from your data, this model should be discussed in the introduction.

Where appropriate, factual information should be referenced using end-notes. When presenting background information, you can guide the reader to a detailed description of a particular item with the statement such as: "*A more detailed discussion of laminar flow can be found elsewhere [1]*". If you know where there is a good discussion of some item, you don't have to repeat it, just guide the reader to the piece.

How one proceeds from this point depends upon whether the paper is about a theoretical study or is a report on an experiment. I will first suggest a format for papers about experimental investigations and then one that describes a theoretical derivation.

Experimental Investigations

THE EXPERIMENT: This section guides the reader through the techniques and apparatus used to generate the data. Schematic diagrams of equipment and circuits are often easier to understand than prose descriptions. A statement such as "*A diagram of the circuit used to measure the stopping potential is shown in Figure 6*" is better than a long elegant set of words. It is not necessary to describe in words what is shown in a diagram unless you feel that there is a very special part which should be pointed out to the reader. If special experimental techniques were developed as part of this work, they should be discussed here. You should separate the discussion of the equipment used to measure something from your results. This section should not include data presentations or discussions of error analysis.

DATA PRESENTATION AND INTERPRETATION OF RESULTS: This is the most important section of the paper. The data are the truths of your work. This section should lead the reader through the data and how errors were measured or assigned. The numerical data values are presented in tables and figures, each with its own number and caption, e.g.. "*The results of the conductivity measurements are shown in Table 3*". It is difficult to follow narratives where the numerical results are included as part of the narrative. Raw, unanalyzed data should not be presented in the paper. All figures and tables should be referred to by their number. Any figure or table that is not discussed in the narrative should be eliminated. Items which are not discussed have no place in a paper.

A Theoretical Study

THE MODEL: This part should consist of a theoretical development of the constructs used to model the physical system

under investigation. Formulae should be on separate lines and numbered consecutively. The letters or symbols used in the equations should be identified in the narrative, e.g.. *The potential can be approximated as:*

$$W \approx Z - \sigma(\rho) \ , \qquad (1)$$

where Z is the number of protons and σ is the screening constant that is dependent on the charge density, ρ, of the inner electrons of the K and L shells. If you wish to use this formula at a later time in the narrative, you refer to it by its number, e.g.. *"The straight line fit shown in Figure 3 means that we can use Equation 1 to extract a value of..."*

CALCULATIONS: This section presents a summary and discussion of the numerical results calculated from the model. The results should be presented in tables or graphs, each with a caption. A table or graph that is not discussed in the narrative should be eliminated. Data that are not interpreted by the writer have no place in a paper. One should reference numerical results that are used in the calculations and come from previous work done by others .

The following sections pertain to both types of papers.

CONCLUSIONS: It is indeed rare that one can come to clear and meaningful conclusions in one paper. I do not know of many papers where this section should be included.

REFERENCES: All references, numbered in order from beginning to end of the paper, are collected together at the end of the paper. You should be aware of the following format:

If the reference is a text-

1. A.J. Smith and Q.C.S. Smythe, Electromagnetic Theory, Addison Wesley, New York, (1962), p. 168.

If the reference is a journal-

2. J. Boswain, Journal of Results, 22, (1968), pp. 122-127.

If the reference is unpublished-

3) R.J. Ralson, private communication.

ACKNOWLEDGMENTS: This short section should acknowledge the help received (that is not referenced in the previous section) from others. This is where you would give credit to a lab partner or someone in the machine shop who helped you build a piece of equipment.

OTHER ADVICE

TABLES AND FIGURES are placed by the layout editors at the corners of the page to make the format attractive and easy to read. Often a figure is not on the same page as the discussion of the figure. Each table or figure should be numbered and have a caption which explains the figure. Readers scan papers by looking at the figures and data tables before they read the narrative of the work. Take care to put enough information in the caption of a figure or table so that the reader can get some feeling for the meaning of the data presentation. All lines shown on graphs should be identified, e.g.. *"The dashed line is drawn to guide the eye"* or *"The solid line is a fit to the data using the Ising model"*

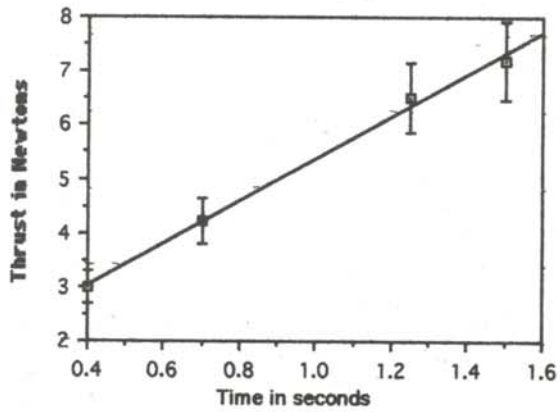

Figure 1

A graph of the measured thrust of a D-2 model rocket engine as a function of time. The line drawn is the least squares fit straight line to the data.

State	Experimental eV	Theoretical eV
3S	5.15±.01	5.13
4S	1.89±.02	1.93
3P	2.96±.02	3.02

Table 1

Energy states found in the numerical search. The accepted values for these states are also listed.

An example of a graph of a set of data is shown in Figure 1. The graph is sized by the range of data points. The bottom left point does not have to be the point (0,0). Error bars are shown with the data points. A graph with all the data points clustered in one small corner and lots of white space does not help the reader get a feeling of the dependence of your data. Be careful that the figures you present are not too busy; too much information on a figure makes it difficult to pick out the important parts.

NUMBERS AND UNITS Any experimentally measured data presented in tables (such as shown in Table 1), should include an uncertainty. You should use scientific notation when presenting numbers, $(7.34 \pm .03) \times 10^7$ eV. Take care that you have the correct number of significant digits in your results; just because the computer prints out 6 digits does not mean that they are significant. You should use the MKS system of units.

STYLE It is often helpful to make a flow chart of your paper before you write it. In this way, you can be sure that the logical development of your presentation does not resemble two octopuses fighting, but that it is linear.

One generally writes the report in the past tense. You already did the experiment. You also should use the third person neuter case. Even though you might have done the work by yourself, you use "we". e.g.. *"We calculated the transition probability for..."* It is often confusing when you begin sentences with conjunctions. Make sure that each sentence is a clear positive statement rather than an apology.

There are a few words or phrases you should be careful of using. ***Fact*** - this is a legal word. I am not sure what it means in physics. ***Proof or prove*** - These words are meaningful in mathematics, but you can't prove something in physics, especially experimental physics. ***The purpose of this experiment is...*** Often it is necessary to do the experiment to complete the requirements for your degree. You do not need to discuss the purposes of the experiment. ***One can easily show that...*** - Don't try to intimidate the reader. What if the reader finds it difficult to show? Remember that the reader of your paper is a senior in college! ***It is obvious that... or One clearly can see....*** - Such statements only intimidate the reader that does not find your work trivial. What is obvious to someone who has spent a lot of time thinking about it may not be obvious to the reader of your paper. *Data* is the plural form of the noun datum. *"The data are ..."* or *"The data show that ...."*

The Journal of Undergraduate Research in Physics

The Journal of Undergraduate Research in Physics is the journal of Sigma Pi Sigma and the Society of Physics Students. It is pproduced by the Physics Department of Guilford College, Greensboro NC 27410. Inquiries about the journal should be sent to the editorial office.

The Journal of Undergraduate Research in Physics **ISSN 0731-3764**

Editorial Office -
The Journal of Undergraduate Research in Physics
Physics Department
Guilford College
Greensboro, NC 27410
336-316-2279 (voice)
336-316-2951 (FAX)

Editor -
Dr. Rexford E. Adelberger
Professor of Physics
Physics Department, Guilford College
Greensboro, NC 27410
Rex@Guilford..Edu

Managing Editor -
Mr. Ari M. Betof
ABetof@Guilford.Edu

The Society of Physics Students

National Office -
Dr. Phillip W. (Bo) Hammer, Director
Ms. Sonja Lopez, SPS Supervisor
Society of Physics Students
American Institute of Physics
One Physics Ellipse
College Park, MD 20740
301-209-3009

President of the Society -
Dr. Gary D. White
Department of Physical Sciences
Northwestern State University of Louisiana

President of Sigma Pi Sigma -
Dr. Thomas Olsen
Department of Physics
Lewis & Clark College

- EDITORIAL BOARD -

tear along dashed line